IEEE Access
Multidisciplinary | Rapid Review | Open Access Journal

Received 11 April 2024, accepted 29 May 2024, date of publication 7 June 2024, date of current version 30 July 2024.

Digital Object Identifier 10.1109/ACCESS.2024.3411090

RESEARCH ARTICLE

Uncoupled Stability and Achievable Impedance Extremes of Haptic Interaction: A Comprehensive Study

SHOULONG WANG[1], JIE ZHAO[1], (Member, IEEE), CHEN YANG[2], (Member, IEEE), AND YANHE ZHU[1], (Senior Member, IEEE)

[1]State Key Laboratory of Robotics and System, Harbin Institute of Technology, Harbin 150080, China
[2]ZJU-Hangzhou Global Scientific and Technological Innovation Center, Zhejiang University, Hangzhou 311215, China

Corresponding author: Yanhe Zhu (yhzhu@hit.edu.cn)

This work was supported in part by the National Key Research and Development Program of China under Grant 2022YFB4700300, in part by the National Natural Science Foundation of China under Grant 92048301, and in part by the National Outstanding Youth Science Fund Project of National Natural Science Foundation of China under Grant 52025054.

ABSTRACT Uncoupled stability analysis is valuable for assessing the stability of haptic interaction, since the interaction between a stable haptic device and a human operator maintains stability. Previous analyses have primarily focused on the normalized parameter space, but they yield an incorrect stability region that may lead to instability in the case of large normalized physical damping (NPD). Additionally, these analyses have neglected to return to the real parameter space, which can result in misconceptions such as increasing the control period expands the stability region or incomplete notions such as increasing the physical inertia always enlarges the stability region. To address these issues, this article presents an uncoupled stability constraint in the normalized parameter space that is applicable for all NPDs. Furthermore, the study returns to the real parameter space and, for the first time, provides analytical expressions that demonstrate the impacts of control period, physical damping and physical inertia on the achievable extremes of virtual stiffness and damping. Remarkably, it is observed that four out of the six influences exhibit non-monotonic behaviors, characterized by an ''increase-decrease-increase'' pattern. The correctness of the developed uncoupled stability region in the normalized parameter space and the existence of the unconventional non-monotonic behaviors in the real parameter space are validated through simulations and experiments.

INDEX TERMS Compliance and impedance control, haptics and haptic interfaces, impedance range, physical human–robot interaction, stability analysis.

I. INTRODUCTION

Hptic devices have found widespread use in physical human-robot interaction (pHRI) applications, including but not limited to rehabilitation [1], [2], robotic surgery [3], [4], [5], space exploration [6], [7], intelligent vehicles [8], [9], [10], [11] and various training systems [12], [13], [14]. These devices enable users to physically interact with virtual environments (VEs) that are either reconstructed from reality or specially designed, providing force feedback that enhance the realism and immersion of the experience. Among all the requirements of a haptic device, interaction stability is the top priority since an unstable behavior can pose a danger to both the robot and the human. However, the interaction stability analysis is challenging as it involves not only the nonlinear factors in the haptic device (such as the sampling, the discretization, the quantization, the Coulomb friction and the delay), but also the time-varying and personal-dependent behaviors of the human operator [15].

In order to address the challenge of interaction stability, considerable efforts have been devoted. These efforts can be broadly categorized into two main strategies. The first

The associate editor coordinating the review of this manuscript and approving it for publication was Zheng Chen.

strategy, i.e. Strategy I, involves isolating the haptic device for analysis, assuming that the human operator possesses specific properties. Representative approaches include passivity analysis, absolute stability analysis, input-to-state stability (ISS) analysis and uncoupled stability analysis. The second strategy, i.e. Strategy II, involves integrating the information of the human operator into the controlled plant so as to relax the requirement on the haptic device when employing certain stability approaches.

The most famous approach using Strategy I is the so-called passivity analysis. By assuming the human operator is passive and limiting the haptic device in the passivity constraint, the stability of the interacted system is guaranteed since the interaction of two passive systems remains passive and thus stable [16]. In [17], necessary and sufficient conditions for the passivity of the general sampled-data haptic device and the concrete impedance-controlled haptic device were obtained. Later the general passivity condition was extended to adapt to both nondelayed and delayed nonlinear VEs by the authors of [18]. The concrete impedance-controlled passivity condition was extended to incorporate delay in [19] and further low-pass velocity filter in [20]. In addition, the passivity condition for both nondelayed and delayed virtual stiffness renderings considering the nonlinear Coulomb friction and quantization effect was derived in [21] and [22]. While these works concentrate on deriving the passivity constraints under different situations, there are also efforts attempting to keep the haptic device in the passivity constraint via online adjustment. The passivity observer/passivity controller (PO/PC) method [23] and the energy-bounding algorithm (EBA) [24] were proposed to dissipate the excessive generated energy in real time by adjustable virtual damping and intrinsic physical damping, respectively. Afterwards, the authors of [25] presented a force-bounding approach (FBA) to directly limit the control force in a range satisfying the passivity condition, thereby ensuring stable interaction with any VE (linear, nonlinear, delayed, etc.). Although the passivity approach is celebrated for the advantages of yielding simple results and exhibiting remarkable robustness, its conservativeness is also well-known.

Another approach utilizing Strategy I is based on the Llewellyn's absolute stability criterion [26]. It can guarantee the stability of the two-port network system by assuming the two terminations are passive. Based on the virtual coupling concept [27], the haptic device can be further divided into two parts: the VE and the virtual coupling, which is a two-port network connecting the human and the VE. Then by assuming both the human and the VE are passive, Llewellyn's absolute stability criterion can be applied to the virtual coupling and the stability of the interaction system is achieved, as done in [28]. The requirement of the absolute stability is less restrictive than that of the passivity since the former only requires the haptic device would not make the passive human unstable while the latter requires the haptic device to be passive. Thus the constraint region resulted from the absolute stability is larger than that of the passivity-based approach.

Recently, ISS [16] was introduced in the haptic area to analyze the interaction stability [29], [30]. Since ISS is equivalent to the dissipativity and passivity is a special case of dissipativity, the stability of the interaction system is guaranteed if assuming the human to be passive and limiting the haptic device to be ISS. It is because the interconnection of two dissipative systems is still dissipative and thus stable [16]. ISS is less restrictive than passivity since it allows some amount of output energy to be extracted from the system while passivity allows none. Thus ISS imposes a much looser constraint in comparison with the case of passivity. In this respect, the study [31] relaxed the passivity condition of the PO/PC method to the ISS condition by permitting the generation of bounded energy, thus extending the achievable impedance range.

The above three approaches raise stricter-than-stable requirements on the haptic device since the interaction of two merely stable systems does not guarantee the overall stability. But there is also another approach [32] only requires the stability of the haptic device (i.e. the uncoupled stability approach) so that it renders the largest constraint region when using Strategy I. This approach is based on the observations that the human operator always helps stabilize the haptic device, as investigated in [19], [22], and [32]. Therefore, the interaction of a stable haptic device with a human operator ensures the interaction stability.

Different from Strategy I, Strategy II integrates the information of the human operator into the controlled plant, thereby loosing the constraint of the haptic device. For example, the human impedance was incorporated into the plant model in [19] and [33] to expand the uncoupled stability region and the passivity region, respectively. According to the strong passivity theorem [16], if the shortage of passivity (SOP) of one subsystem is less than the excess of passivity (EOP) of the other subsystem, the overall system remains passive and stable. Hence, the EOP of the human was identified and utilized to achieve larger impedance rendering in methods such as the PO/PC method [34] and the FBA method [35]. Moreover, the bounded nature of the human impedance was exploited to loose the constraint of the haptic device when applying the absolute stability [36] or the small gain theorem [37].

By comparing the above two strategies, we can see that while Strategy II can provide larger stability region, it is more complex since it requires to identify the information of the human and should carefully adjust the controller if the human behaves differently (e.g. suddenly releases the haptic device) or changes to another one. On the contrary, Strategy I is simpler and more robust to the human variation. Furthermore, among all the approaches in Strategy I, the uncoupled stability approach renders the largest region since it only needs the stability of the haptic device without any

further requirements, and thus is the main concern of this article.

A. PRIOR WORK

Extensive works have contributed to the analysis of the uncoupled stability of the haptic interaction. Despite earlier works [17], [38] touching this issue by numerical calculations, it was first analyzed theoretically in [32]. In this article, the haptic device was modeled as an impedance-controlled damped system considering the factors of sampling and discretization. The sampled-data system was first transformed to the discrete-time domain and then the continuous-time domain, where the classical Routh-Hurwitz stability criterion was applied to get the stability constraint. An approximate linear constraint was also proposed when the virtual damping was sufficiently small. However, as real parameters were used in the derivation, the resulting explicit stability inequality was so complex that even the boundary curve was hard to distinguish. Besides, since only a portion of the Routh-Hurwitz stability criterion was utilized, the resulting stability constraint was not accurate. When the plant has large normalized physical damping (NPD) δ (an item explained in Section II), a rendered impedance far inside the stability boundary can lead to instability, as presented in Section V. This happens because a linear stability inequality is missing in Gil's result when δ is large.

The authors in [39] noticed this additional linear stability constraint through numerical calculations and reported that it occurred when $\delta > 2.3$. However, the reason is still unclear. Another contribution of [39] was the introduction of the normalized parameters (detailed in Section II), which transformed the system from the real parameter space to the normalized parameter space. This transformation reduced the number of system parameters and greatly simplified the stability analysis. Using this technique, [39] and [40] extended the uncoupled stability analysis to the impedance-controlled damped system with delay. While the former numerically investigated the influences of δ and delay on the stability boundary in a wide δ range, the latter proposed an analytical approximate stability constraint with delay for small δ and small virtual damping. However, there is still a lack of a correct and explicit stability constraint applicable for a wide range of δ.

Later on, other factors are included into the framework of uncoupled stability analysis. In [19], the authors extended the uncoupled stability analysis to the system with physical stiffness by incorporating the physical inertia, damping, and stiffness of the human operator into the controlled plant. Through numerical analysis, they found that with small physical stiffness, the stability region of the system in the normalized space became larger. The work of [20] included the velocity filter into the uncoupled stability analysis, indicating that more aggressive low-pass filtering (reducing the cut-off frequency or increasing the filter order) reduced the stability region. Another effort [41] compared the uncoupled stability constraints for various discrete implementations of the impedance controller when either position or velocity was sampled. It was found that velocity-sampled approach provided a larger stability region. The authors of [42] significantly expanded the uncoupled stability region by using analog position feedback, but at the cost of a more complex system configuration. Recently in [43], the virtual mass control was included into the framework of uncoupled stability analysis and the stability constraints of all seven types of control combinations were investigated.

Apart from analyzing the sampled-data system in the discrete-time domain, there are also studies conducted in the continuous-time domain. For instance, in [44], the authors converted the discrete-time impedance controller to its continuous-time equivalent and determined the stability boundary using continuous-time analysis tools. The simulations and experiments verified that the result applied for the case where the virtual damping was small or the delay was large when δ was small. But if the virtual damping is large and no delay involves, the stability region is conservative. In light of their study, the authors of [45] achieved an expanded stability region by replacing the viscous friction model with the Gaussian friction model.

According to the literature review, the correct uncoupled stability constraint for large δ is still lacking. The existing stability constraint may lead to instability behaviors in the case of large δ. Besides, the analytical formulas showing the influences of the physical parameters (control period, physical damping, and physical inertia) on achievable impedance range are in the absence. The existing conclusions drawn from limited experiments might be questionable. For example, the authors in [46] indicated that the larger the mass the larger the stability region by performing the comparative experiments with different masses. However, there are also cases that the larger the inertia, the smaller the achievable maximum stiffness, as experimentally shown in Section V. Then in these cases, the intention to increase the maximum stiffness will instead result in its unexpected reduction if guided by existing conclusion. In this scenario, this article derives the analytical uncoupled stability constraint applicable for all NPDs, thereby eliminating the instabilities that might induced by existing stability constraint. Besides, the influences of the physical parameters on the achievable impedance extremes are analytically investigated so that accurate conclusions of these influences are obtained.

B. CONTRIBUTIONS

The contributions of this work are summarized as follows. Firstly, the complete version of the uncoupled stability constraint in the normalized parameter space is obtained, whereas the existing stability constraint is only applicable for low NPDs. It incorporates an additional linear constraint and thus eliminates the instability behaviors that might be instructed by the existing stability constraint. Furthermore,

the complete stability constraint results in several new insights that contradicts with traditional thinking.

Secondly, utilizing the newly established stability constraint, we formulate the analytical expressions for the achievable impedance extremes within the normalized parameter space, whereas the existing analytical expressions have not yet been established. Additionally, linear approximation formulas for several specific scenarios are provided.

Finally, we shift the stability analysis back to the real parameter space, which offers more intuitive conclusions comparing to the existing analyses conducted in the normalized parameter space. Analytical expressions showing the influences of the real physical parameters (control period, physical damping, and physical inertia) on the achievable impedance extremes are obtained for the first time. While previous efforts only provide limited experimental results and suggest monotonic behavior, it is found that contrary to the conventional thinking, not all the influences are monotonic. Increasing the physical inertia results in an "increase-decrease-increase" pattern of achievable maximum stiffness. Similarly, reducing the control period, increasing the physical damping or the physical inertia leads to an "increase-decrease-increase" pattern of achievable maximum damping. Therefore, when determining the real physical parameters in the design of the haptic device with the aim of achieving the largest possible impedance range at the lowest possible cost, an overall consideration should be conducted.

C. PAPER ORGANIZATION

The remainder of the article is organized as follows. Section II describes the considered system and obtains the stability constraint applicable for all NPDs in the normalized space. Then analytical expressions for the achievable impedance extremes within the same space are formulated in Section III. Afterwards, Section IV returns to the real parameter space to see the influences of the real physical parameters on the achievable impedance extremes. Simulations and experiments are presented in Section V, verifying the aforementioned theories. Section VI concludes this article and provides future research directions. At last, the derivations of the properties of two newly defined functions, the stability constraint in the normalized parameter space and the monotonicity analysis of the function of achievable maximum virtual damping v.s. δ are attached in three appendices, respectively.

II. UNCOUPLED STABILITY ANALYSIS OF HAPTIC INTERACTION IN NORMALIZED PARAMETER SPACE

In this section, the model of the impedance-controlled haptic device is established in the real parameter space and then transformed to the normalized parameter space. By using two newly defined functions, we can simplify the stability analysis and finally obtain the complete uncoupled stability constraint.

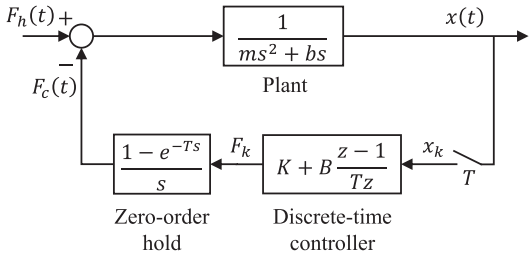

FIGURE 1. Model of the impedance-controlled haptic device.

A. SYSTEM MODELING

In a haptic interaction scenario, incorporating all influencing factors such as human dynamics and nonlinearities like time discretization, position quantization, actuator saturation, Coulomb friction, and loop delays would make stability analysis infeasibly complex. Previous studies have shown that Coulomb friction can dissipate the energy introduced by quantization [21], [22], and human dynamics tend to stabilize the system [19], [22], [32]. Thus, these factors can be excluded. Additionally, actuator saturation and loop delays are omitted so as to focus on the stability conditions related to time discretization, which is often the primary source of instability in haptic systems. Consequently, the impedance-controlled haptic device is modeled as a sampled-data system as shown in Fig. 1. The controlled plant is a rigid body (m) with some physical damping (PD) (b). Its position (x) is sampled with a sampling period T and sent to the discrete impedance controller

$$H(z) = K + B\frac{z-1}{Tz}, \tag{1}$$

where K and B are the virtual stiffness (VS) and the virtual damping (VD), respectively. Then the controller output F_c, which passes through a zero-order hold (ZOH), is combined with the human force F_h as the input of the plant, so as to generate the motion. In this article, the parameters m and T are assumed to be positive, while b is assumed to be non-negative to include the case of the control of an undamped plant ($b = 0$) for generality.

Though the system seems to be clear and simple, its stability is not easy to analyze. The major difficulty lies in its sampled-data nature which combines both the continuous (the plant) and the discrete (the controller) parts. As a result, neither the Routh-Hurwitz stability criterion developed for the continuous-time system nor the Jury stability criterion developed for the discrete-time system can be directly applied to perform the stability analysis. But if we assume the human force F_h to be constant during one sampling period [19], the continuous-time plant can be transformed into the discrete-time domain and then the sampled-date system becomes a pure discrete-time system. Consequently, the tools developed for the stability analysis of the discrete-time system can be used.

Another difficulty in analyzing the stability is the numerous parameters. The stability analysis eventually leads to

a set of inequalities that all these system parameters must satisfy. As shown in Fig. 1, there are five parameters: three physical parameters m, b, and T, and two control parameters K and B. With five parameters, the resulted inequalities are inevitably cumbersome, as shown in [32]. This hinders further investigations. To simplify the derivation process and obtain a clear explicit constraint, the normalization rule developed in [39] is adopted to group some of the real parameters to reduce the amount of the analyzed parameters.

B. NORMALIZATION OF SYSTEM MODEL

The normalization rule developed in [39] reduces these five real parameters to three dimensionless parameters: the normalized physical damping (NPD) $\delta = bT/m$, the normalized virtual stiffness (NVS) $\alpha = KT^2/m$, and the normalized virtual damping (NVD) $\beta = BT/m$. It can be seen that $\delta = 0$ if and only if $b = 0$, indicating the case of controlling an undamped plant. After the normalization, the system has transformed from the real parameter space to the normalized parameter space. The normalized characteristic equation will be derived in the following.

First of all, the continuous part of the system, i.e. the plant with ZOH, is discretized as

$$\begin{aligned} G(z) &= \frac{z-1}{z}\mathcal{Z}\left[\frac{1}{ms^3+bs^2}\right] \\ &= \frac{T^2}{2m}\frac{c_{\delta 1}(\delta)z + c_{\delta 2}(\delta)}{z^2-(1+e^{-\delta})z+e^{-\delta}}, \end{aligned} \tag{2}$$

where

$$c_{\delta 1}(\delta) = \begin{cases} \dfrac{\delta - 1 + e^{-\delta}}{\frac{\delta^2}{2}}, & \text{if } \delta > 0, \\ \lim\limits_{\delta\to 0}\dfrac{\delta - 1 + e^{-\delta}}{\frac{\delta^2}{2}} = 1, & \text{if } \delta = 0, \end{cases} \tag{3}$$

and

$$c_{\delta 2}(\delta) = \begin{cases} \dfrac{1 - e^{-\delta} - \delta e^{-\delta}}{\frac{\delta^2}{2}}, & \text{if } \delta > 0, \\ \lim\limits_{\delta\to 0}\dfrac{1 - e^{-\delta} - \delta e^{-\delta}}{\frac{\delta^2}{2}} = 1, & \text{if } \delta = 0, \end{cases} \tag{4}$$

are two newly proposed functions of δ, defined for the simplification of the stability derivation. Properties of these two functions are derived in Appendix A. It is shown that both of them are monotonically decreasing functions and in the range $(0, 1]$ when $\delta \in [0, \infty)$. Besides, $c_{\delta 1}(\delta) \geq c_{\delta 2}(\delta)$ and "=" is true if and only if $\delta = 0$. For compactness, they are represented by $c_{\delta 1}$ and $c_{\delta 2}$ in the following.

Then the system's discrete-time closed-loop transfer function can be obtained:

$$G_{cl}(z) = \frac{G(z)}{1 + H(z)G(z)} = \frac{p_n(z)}{p_d(z)}, \tag{5}$$

where

$$p_n(z) = \frac{T^2}{m}c_{\delta 1}z^2 + \frac{T^2}{m}c_{\delta 2}z \tag{6}$$

and

$$p_d(z) = 2z^3 + a_1z^2 + a_2z - c_{\delta 2}\beta \tag{7}$$

in which

$$\begin{aligned} a_1 &= c_{\delta 1}(\alpha + \beta) - 2(1 + e^{-\delta}) \\ a_2 &= c_{\delta 2}\alpha + (c_{\delta 2} - c_{\delta 1})\beta + 2e^{-\delta} \end{aligned}$$

are the numerator polynomial and the denominator polynomial, respectively. Hence, the normalized characteristic equation of the closed-loop system is

$$p_d(z) = 0. \tag{8}$$

This coincides with the results in [32] and [39] if no delay involves, but has a simpler form due to the introduction of the functions $c_{\delta 1}$ and $c_{\delta 2}$. The introduction of these two functions not only simplifies the presentation of the transfer functions, but also simplifies the derivation of the stability constraint, as will be seen in the following subsection.

C. UNCOUPLED STABILITY ANALYSIS

The discrete-time system is stable if and only if all the characteristic roots are inside the unit circle in the z-plane. In [32] and [43], the discrete-time system was transformed to the continuous-time domain to perform the stability analysis by using the Routh-Hurwitz criterion. This method is quite complicated, but it can obtain the same final results as the method we used below. However, the authors only used part of the Routh-Hurwitz criterion, resulting in a necessary condition for the stability, which is applicable only to situations with small δ. This happens perhaps because of the complexity in the derivation. In the following, we will use the Jury criterion, which is developed to directly analyze the stability of the discrete-time system, to get the sufficient and necessary condition for the system stability.

Applying the Jury stability criterion to the normalized characteristic equation (8), we can get the stability constraint of the normalized system:

$$\begin{cases} p_d(1) & > 0 \\ p_d(-1) & < 0 \\ 2 & > c_{\delta 2}|\beta| \\ 4 - c_{\delta 2}^2\beta^2 & > |2a_2 + c_{\delta 2}\beta a_1| \end{cases}. \tag{9}$$

After some mathematical manipulations, the explicit constraint is derived in (10). The details of the derivation are given in Appendix B.

$$\begin{cases} \beta & > -\delta \\ 0 < \alpha & < f(\beta) \\ \alpha & < \dfrac{4(1+e^{-\delta})}{c_{\delta 1} - c_{\delta 2}} - 2\beta \end{cases} \tag{10}$$

where

$$f(\beta) = \frac{-(c_{\delta 1} + c_{\delta 2})c_{\delta 2}\beta^2 + 2(c_{\delta 1} + e^{-\delta}c_{\delta 2})\beta + 4(1 - e^{-\delta})}{(c_{\delta 1}\beta + 2)c_{\delta 2}} \tag{11}$$

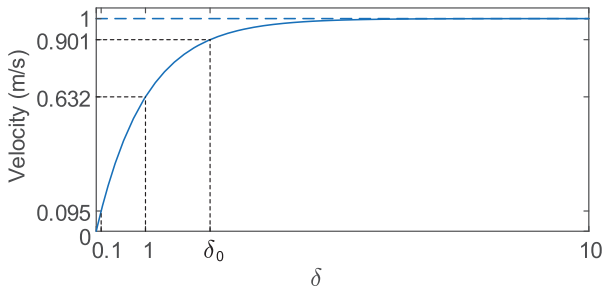

FIGURE 2. Unit step response of a first-order system. δ_0 represents a 90.1% completion rate of the step response in one sampling period.

and $\alpha = f(\beta)$ represents a hyperbola in the $\beta - \alpha$ plane. It is worth noting that the introduction of the intermediate functions $c_{\delta 1}$ and $c_{\delta 2}$ greatly reduces the complexity of the derivation.

Moreover, with $\delta_0 \approx 2.311$ being the solution of (58), the stability constraint (10) can be further divided into the following two cases:

1) if $\delta \leq \delta_0$

$$\begin{cases} \beta & > -\delta \\ 0 < \alpha & < f(\beta) \end{cases}, \tag{12}$$

2) if $\delta > \delta_0$

$$\begin{cases} \beta & > -\delta \\ 0 < \alpha & < f(\beta) \\ \alpha & < \dfrac{4(1+e^{-\delta})}{c_{\delta 1} - c_{\delta 2}} - 2\beta \end{cases}. \tag{13}$$

Since the NPD δ is the ratio of the control period (T) to the mechanical time constant of the plant ($\tau_m = m/b$), it also represents the completion rate of the step response in one sampling period. As indicated in Fig. 2, if δ is small (e.g. $\delta = 0.01$), i.e. the completion rate is low, the speed increases linearly in one sampling period. If δ is large (e.g. $\delta = 100$), the transient period is so short that the speed can be considered as a constant in one sampling period. If δ is in between, the response of the speed in one sampling period is the typical step response of a first-order system with different completion rate. δ_0, which indicates T is δ_0 times τ_m, represents the completion rate of 90.1%. Therefore, the results (12) and (13) imply that when $\delta > \delta_0$, i.e. the completion rate is more than 90.1%, there will be an additional linear inequality constraining the stability region from the right. Fig. 3 and Fig. 4 show the stability constraints under different values of δ. Specifically, Fig. 3 shows the stability region on a larger scale, while Fig. 4 focuses on the cases around δ_0.

Remark 1: The stability constraint obtained in previous works [32], [43] is (12), which is only applicable for the case $\delta \leq \delta_0$. When it is used to analyze the stability of a system with large NPD, the control parameters satisfying it could lead to instability, as verified through simulations and experiments in Section V. This situation becomes even worse

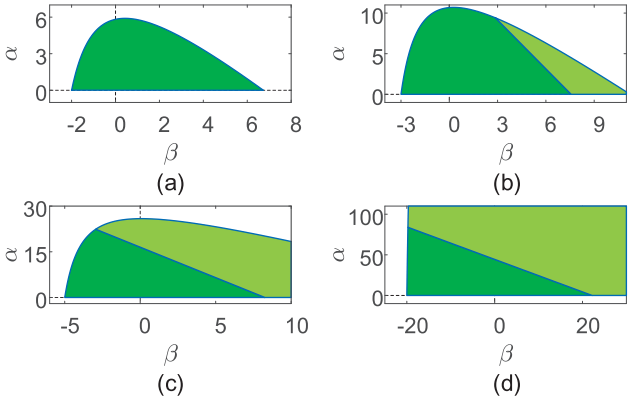

FIGURE 3. Stability constraint (12) and (13) (the dark green region) with the comparison with that in [43] (the dark green region plus the light green region) under different values of δ. (a) $\delta = 2 \leq \delta_0$, (b) $\delta = 3 > \delta_0$, (c) $\delta = 5 > \delta_0$, and (d) $\delta = 20 > \delta_0$.

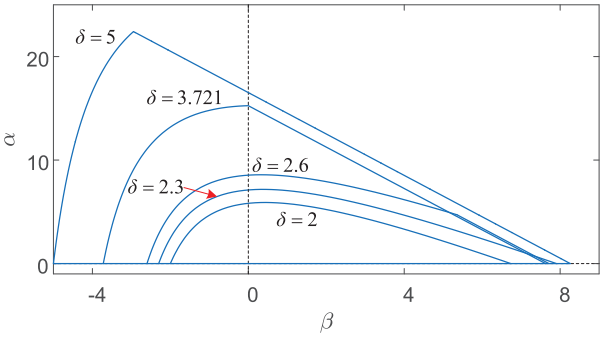

FIGURE 4. Stability constraint around δ_0.

when the NPD is larger, as shown in Fig. 3. This occurs because their result lacks a linear constraint (the third inequality in (13)) that constrains the stability region from the right when $\delta > \delta_0$. In [39], this linear constraint was discovered by numerical calculations. It was found that when $\delta > 2.3$, a line with a slope of -0.5 (in the $\alpha - \beta$ plane) appeared limiting the stable region. In fact, it is precisely the boundary line of the third inequality in (13). The newly proposed stability constraints (12) and (13) extend the applicability to cover all NPDs, thereby addressing the limitations of previous analyses. The additional linear constraint complicates the analysis of the stability boundaries, as will be seen in the next subsection.

D. DISCUSSIONS ON STABILITY REGION

The primary concern is how the stability region changes with the physical properties of the system. Fig. 3 and Fig. 4 illustrate that generally, a larger NPD leads to an expanded stability region. Yet, a notable exception exists. As Fig. 4 demonstrates, when δ is slightly larger than δ_0, while the stability region expands in other directions with an increase in δ, its right side first contracts and then expands due to the previously mentioned additional linear constraint. This results in an unusual phenomenon that a system may be

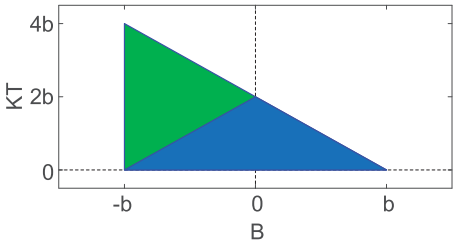

FIGURE 5. Comparison of the uncoupled stability (the green region plus the blue region) and the passivity (the blue region) when δ is large enough.

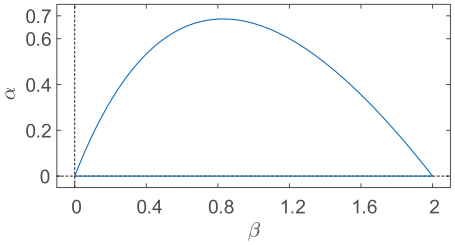

FIGURE 6. Stability constraint when $\delta = 0$.

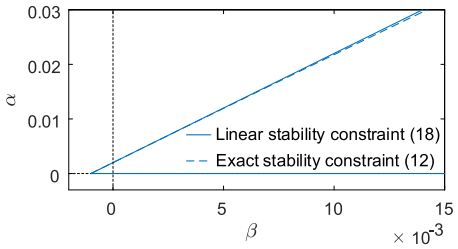

FIGURE 7. Comparison between the linear stability condition (18) and the exact stability constraint (12) when $\delta = 0.001$.

stable at lower NPD but unstable at higher NPD, challenging the conventional belief that greater damping ensures more stability.

Another noteworthy point is that for large enough NPD, the stability region still positions the passivity region as conservative, challenging the conclusion drawn by Colgate and Schenkel [17]. When $\delta \to \infty$, the stability region simplifies to a triangular shape as defined by:

$$\begin{cases} \beta & > -\delta \\ 0 < \dfrac{\alpha}{2} & < \delta - \beta \end{cases}. \tag{14}$$

Transformed into the real parameter space, this implies:

$$\begin{cases} B & > -b \\ 0 < \dfrac{KT}{2} & < b - B \end{cases}. \tag{15}$$

Comparing it to the passivity constraint (16), as shown in Fig. 5, the finding in [17] that the uncoupled stability region converges on the passivity region when δ is large enough is only applies to the case $B > 0$. When examining the whole uncoupled stability region, passivity is still conservative.

$$0 < \frac{KT}{2} < b - |B|. \tag{16}$$

In addition, the uncoupled stability criterion allows for a higher mmax-NVS[1] value, up to twice that of the passivity constraint when $\delta \to \infty$.

Moreover, in scenarios where NPD is negligible (i.e. $\delta \to 0$), diverging from previously used complex numerical calculations or various approximation techniques [38], [40], [47], we introduce a simpler and direct method. This method treats such scenarios as merely special cases of the general stability constraint, giving two simplified stability constraints based on the necessity of large NVD:

i) If large NVD is necessary, the stability constraint of zero NPD can effectively represent those of near-zero NPDs, since changes of stability regions are minimal for $\delta \to 0$. Substituting $\delta = 0$ into (12), the stability constraint of zero NPD can be obtained:

$$\begin{cases} \beta & > 0 \\ 0 < \alpha & < \dfrac{-2\beta^2 + 4\beta}{\beta + 2} \end{cases}. \tag{17}$$

This is a complete constraint related to α and β, with Fig. 6 illustrating the stability region.

ii) If only small NVD is necessary (i.e. $\beta \to 0$), a linear stability constraint serves as an effective simplification. This is based on the observation of the near-linear α-β relationship in these cases, as evidenced by the dashed curve in Fig. 7, plotting the exact stability constraint for $\delta = 0.001$ and $\beta \to 0$. According to i), Fig. 7 can be viewed as the zoom-out of the origin in Fig. 6. Substituting $\delta \to 0$ and $\beta \to 0$ into (12) yields a stability constraint with a linear upper boundary

$$0 < \frac{\alpha}{2} < \delta + \beta. \tag{18}$$

It is a simple local constraint related to α and β, as illustrated by the solid line in Fig. 7, plotting this constraint for $\delta = 0.001$. An important conclusion in this case is that the NVD and the NPD affect the stability in an exactly the same manner. Note, however, the linear stability condition (18) and the corresponding conclusion hold only for the scenario where both the NPD and the NVD are small, which is a very small area comparing to the whole stability region. Otherwise, either of them breaks, the conclusion is invalid. For example, if only NPD is small, Fig. 6 shows that when β is large (e.g. $\beta > 1$), increasing NVD leads to a decrease of NVS. Conversely, if only NVD is small, Section III-B-I) demonstrates that the increase of NVS along NPD is no longer linear, but in a more complex manner.

[1]Mmax-NVS represents the maximum NVS the haptic device can render, while max-NVS represents the maximum NVS when implementing certain NVD. In other words, mmax-NVS is the maximum of the max-NVS. Other mmin-xx/min-xx or mmax-xx/max-xx follows the same logic.

Furthermore, keeping the NPD constant, we examine the mutual impacts between NVD and NVS on each other's range. Fig. 3 shows that increasing the NVS narrows the NVD range. Conversely, NVD's impact on NVS range is more complex: initially, increasing NVD expands the NVS range up to mmax-NVS, then it shrinks. Additionally, each NVD increase contributes diminishingly to NVS range, since the derivative $\alpha'(\beta)$ decreases. Notably, it's observed for the first time that there are cases where adding positive NVD linearly reduces the range of NVS and only decreasing the NVD to negative values can increase the range of NVS. As detailed in Section III-B-I), these cases occur when $\delta > \delta_2 \approx 3.721$.

III. ACHIEVABLE IMPEDANCE EXTREMES IN NORMALIZED PARAMETER SPACE

This section investigates the range of the achievable NVS and NVD of the haptic device.

A. LOWER IMPEDANCE EXTREMES

Fig. 3 indicates that the mmin-NVS should be larger than 0 (i.e. $K > 0$), indicating a non-negative apparent stiffness (AS). Similarly, the mmin-NVD should be larger than $-\delta$ (i.e. $B > -b$), indicating a non-negative apparent damping (AD, which equals PD plus VD). Both cases are understandable since negative stiffness or damping will lead to physical instability.

In addition, while the mmin-NVS may occur with many values of NVD, the mmin-NVD occurs only at $\alpha = 0$ (except for the case $\delta \to \infty$). This implies that if some stiffness effect is favorable, there must be certain AD effect accompanied. In other words, the emulation of a pure stiffness is impossible.

B. HIGHER IMPEDANCE EXTREMES

1) MMAX-NVS OF THE HAPTIC DEVICE

The mmax-NVS of the haptic device is investigated in this subsection. The corresponding NVD is also given.

The mmax-NVS is the α component of the upmost point in the stability region. We can see from Fig. 3 that if δ is small, the mmax-NVS achieves at the upmost point of the hyperbolic constraint (see Fig. 3(a) and (b)); while if δ is large, the mmax-NVS achieves at the intersection point of the linear constraint and the hyperbolic constraint (see Fig. 3(c) and (d)). The demarcation case occurs when the intersection point of the linear constraint and the hyperbolic constraint coincides with the uppermost point of the hyperbolic constraint.

As the equation of the hyperbolic constraint is $\alpha = f(\beta)$ with $\alpha > 0$ and $\beta > -\delta$, the upmost point is the point that satisfies $f'(\beta) = 0$. Note it as (α_1, β_1), then it can be solved to be:

$$\alpha_1 = \frac{2\left[c_{\delta 1} + c_{\delta 2} - \sqrt{c_{\delta 2}\left(e^{-\delta}c_{\delta 1} + c_{\delta 2}\right)}\right]^2}{c_{\delta 1}^2 c_{\delta 2}}, \tag{19}$$

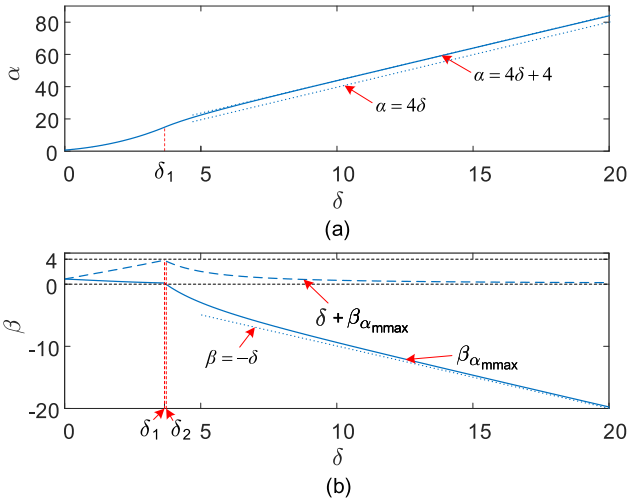

FIGURE 8. (a) Mmax-NVS and (b) the corresponding NVD and NAD.

$$\beta_1 = -\frac{2}{c_{\delta 1}}\left(1 - \sqrt{\frac{e^{-\delta}c_{\delta 1} + c_{\delta 2}}{c_{\delta 2}}}\right). \tag{20}$$

The intersection point of the linear constraint and the hyperbolic constraint has been derived in (66) in Appendix B. Note it as (α_2, β_2), then

$$\alpha_2 = \frac{8[c_{\delta 1} - (2 + e^{-\delta})c_{\delta 2}]}{(c_{\delta 1} - c_{\delta 2})^2}, \tag{21}$$

$$\beta_2 = \frac{2[(3 + e^{-\delta})c_{\delta 2} - (1 - e^{-\delta})c_{\delta 1}]}{(c_{\delta 1} - c_{\delta 2})^2}. \tag{22}$$

The critical case happens when (α_1, β_1) and (α_2, β_2) are the same point. Numerically solving the equation

$$\beta_1 = \beta_2, \tag{23}$$

we can get the critical NPD $\delta_1 \approx 3.659$. Therefore, the mmax-NVS that the haptic device can render is

$$\alpha_{\text{mmax}} = \begin{cases} \alpha_1, & \text{if } \delta \le \delta_1, \\ \alpha_2, & \text{otherwise}, \end{cases} \tag{24}$$

with the corresponding NVD being

$$\beta_{\alpha_{\text{mmax}}} = \begin{cases} \beta_1, & \text{if } \delta \le \delta_1, \\ \beta_2, & \text{otherwise}. \end{cases} \tag{25}$$

The figure of the mmax-NVS v.s. NPD is shown in Fig. 8(a), while the corresponding NVD and NAD v.s. NPD is shown in Fig. 8(b).

From Fig. 8 we can see that the larger the NPD, the larger the mmax-NVS. Besides, it is worth noting that when achieving the mmax-NVS, the NVD is not always positive. Specifically, as derived in Remark 2, when $\delta > \delta_2 \approx 3.721$, the NVD should be negative to achieve the mmax-NVS. Additionally, in order to achieve the mmax-NVS, though the NPD varies significantly along the variation of δ, the NAD is bounded in (0, 4), and approaches 0 when $\delta \to \infty$.

When $\delta \to 0$, from (24) and (25), we can know that $\alpha_{\text{mmax}} \to 12 - 8\sqrt{2}$ (≈ 0.686) with $\beta_{\alpha_{\text{mmax}}} \to 2\sqrt{2} - 2$ (≈ 0.828). Moreover, when $\delta \to \infty$, from (14) we can get

$$\alpha_{\text{mmax}} \to 4\delta, \ \beta_{\alpha_{\text{mmax}}} \to -\delta. \tag{26}$$

It can be seen that in order to achieve the mmax-NVS, the NVD should cancel out all the NPD. In other words, if one wants to achieve the NVS as large as possible when $\delta \to \infty$, the NAD has to be as small as possible. On the other hand, if δ is not that large (e.g. $\delta > 10$), it can be derived from (24) that $4\delta + 4$ is a more accurate approximation of α_{mmax} while 4δ is conservative, as shown in Fig. 8(a).

Remark 2: The following examines to what extent the mmax-NVS of the impedance control is larger than that of the PSC.

Substituting $\beta = 0$ into the stability constraint of the impedance control (10), we can get the stability constraint of the PSC ($H(z) = K$):

$$0 < \alpha < \min\left\{\frac{2(1-e^{-\delta})}{c_{\delta 2}}, \frac{4(1+e^{-\delta})}{c_{\delta 1} - c_{\delta 2}}\right\} \tag{27}$$

By numerical calculations, we can obtain that when $\delta \le \delta_2 \approx 3.721$

$$\frac{2(1-e^{-\delta})}{c_{\delta 2}} \le \frac{4(1+e^{-\delta})}{c_{\delta 1} - c_{\delta 2}}. \tag{28}$$

Therefore, (27) can be further divided into:

$$\begin{cases} 0 < \alpha < \dfrac{2(1-e^{-\delta})}{c_{\delta 2}}, & \text{if } \delta \le \delta_2, \\ 0 < \alpha < \dfrac{4(1+e^{-\delta})}{c_{\delta 1} - c_{\delta 2}}, & \text{if } \delta > \delta_2. \end{cases} \tag{29}$$

As the additional linear stability appearing from right, while it influences the general case from δ_0, it influences the PSC (the intersection of the general case and the α axis) from δ_2. Fig. 9(a) shows the stability region of the PSC, which is under the dashed curve.

For comparison, the mmax-NVS of the impedance control is also plotted in Fig. 9(a) as a solid line. Although both curves increase monotonically along δ, the mmax-NVS of impedance control is larger than that of the PSC. It indicates that NVD plays a positive role in enlarging the mmax-NVS, unlike the negative role played by NVS in enlarging the mmax-NVD, as discussed in Section II-D. In particular, when δ is small, from Fig. 9(b) it can be seen that, adding damping control can greatly increase the mmax-NVS comparing to the PSC. When δ is large, adding damping control can also achieve at least two times the mmax-NVS of the PSC. But for a short interval before δ_2, the mmax-NVSs of the impedance control and the PSC are close, since in these cases the NVDs to achieve the mmax-NVSs are around 0.

2) MMAX-NVD OF THE HAPTIC DEVICE

Given that both the mmin-NVD and the mmax-NVD occur when the NVS equals zero, as illustrated in Fig. 3, the achievable damping range of the impedance control is also

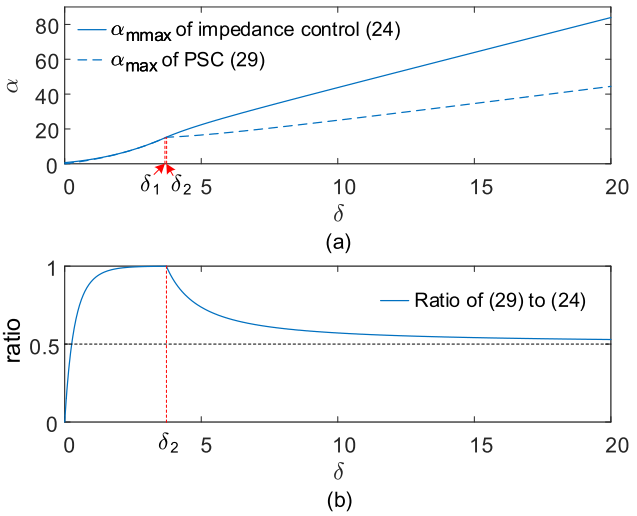

FIGURE 9. (a) Comparison of the mmax-NVSs between the impedance control and the PSC. (b) The ratio of the latter to the former.

the range of the pure damping control (i.e. $\alpha = 0$). The applications of the pure damping control can be found in areas where energy-storing property is undesirable [48], [49].

From (10) we know that $\alpha = 0$ does not satisfy the stability constraint. But if we substitute $\alpha \to 0$ into the stability constraint (10), we can get the approximate stability constraint of the pure damping control $H(z) = B\frac{z-1}{Tz}$, as shown in (30).

$$-\delta < \beta < \min\left\{\frac{2}{c_{\delta 2}}, \frac{2(1+e^{-\delta})}{c_{\delta 1} - c_{\delta 2}}\right\} \tag{30}$$

As derived in Appendix B-A,

$$\frac{2}{c_{\delta 2}} \le \frac{2(1+e^{-\delta})}{c_{\delta 1} - c_{\delta 2}}, \text{ if } \delta \le \delta_0. \tag{31}$$

Therefore, (30) can be further detailed to:

$$\begin{cases} -\delta < \beta < \dfrac{2}{c_{\delta 2}}, & \text{if } \delta \le \delta_0, \\ -\delta < \beta < \dfrac{2(1+e^{-\delta})}{c_{\delta 1} - c_{\delta 2}}, & \text{if } \delta > \delta_0. \end{cases} \tag{32}$$

The stability regions of the NVD and the NAD of the pure damping control, i.e. the achievable NVD and NAD range of the haptic device, are shown in Fig. 10(a) and (b), respectively.

From Fig. 10(a), it can be seen that generally the larger the NPD, the larger the mmax-NVD, except for the values slightly larger than δ_0. The mmax-NVD decreases a little bit in this interval due to the appearance of the additional linear constraint. Thus if one wants to use a small δ to achieve the mmax-NVD as large as possible, δ_0 is the best choice. Besides, when $\delta \to 0$, $\beta_{\text{mmax}} \to \frac{4}{3}\delta + 2$. Accordingly, different from the PSC case, even though there is no physical damping, the system can emulate certain damping effect. Moreover, when $\delta \to \infty$, from (14), we can easily know that $\beta_{\text{mmax}} \to \delta$, indicating a linear dependency between β_{mmax}

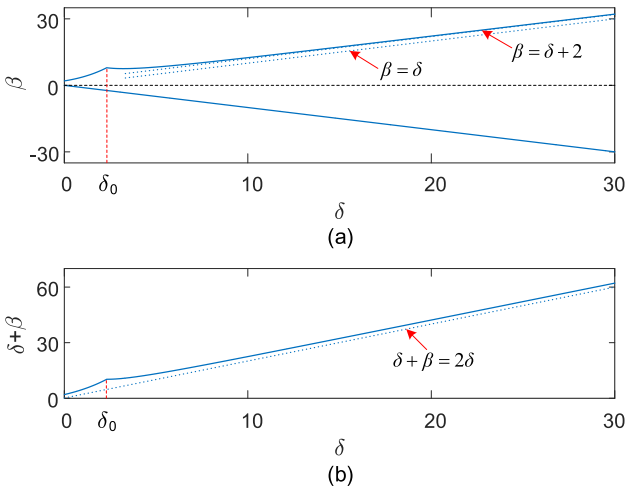

FIGURE 10. Achievable (a) NVD and (b) NAD extremes of the haptic device.

and δ when δ is large. But if δ is not that large (e.g. $\delta > 10$), it can be derived from (32) that $\delta + 2$ is a more accurate approximation while δ is conservative, as shown in Fig. 10(a). All the conclusions are suitable for the mmax-NAD, except an additional δ should be added. One thing is notable that the mmax-NAD the haptic device can render is at least 2 times the NPD.

IV. ACHIEVABLE IMPEDANCE EXTREMES IN REAL PARAMETER SPACE

By far we have resolved the uncoupled stability problem in the normalized parameter space by showing what the stability region is and how it changes when δ varies. However, in practice, the relationships of parameters in the real parameter space are the ultimate concern. Nevertheless, directly extending conclusions from the normalized parameter space to the real parameter space tends to lead to inaccurate results. For example, in Section II it has been shown that in general an increase in δ corresponds to a larger stability region. Therefore, based on $\delta = \frac{bT}{m}$, it tends to believe that the larger the T the larger the stability region or the smaller the m the larger the stability region. However, contrary to the former conclusion, practical experiences have shown that increasing the control period actually reduces the stability region. As for the latter one, it is still an open issue. But there has been a study [46] indicating that increasing the m increases the stability region by performing the comparative experiments with different masses. Therefore, it is necessary to figure out how physical parameters influence the stability region in the real parameter space, which is the focus of this section.

However, since there are five parameters related in the real parameter space, it is not easy to get the compact expressions of K and B v.s. m, b, and T like (12) and (13) as done in the normalized parameter space. Instead, the influences of m, b, and T on achievable impedance extremes are analyzed. Furthermore, there is no need discussing mmin-VS and mmin-VD since from (12) and (13) we know that $\alpha > 0$ and $\beta > -\delta$, indicating $K > 0$ and $B > -b$, regardless of m and T. Therefore in the following will see how the physical parameters m, b, and T influence the mmax-VS and the mmax-VD.

A. MMAX-VS AND ITS RELATIONSHIP WITH M, B, AND T

The direct method to analyze the influence of m, b, and T on K_{mmax} is to substitute $\alpha_{\text{mmax}} = K_{\text{mmax}}T^2/m$ and $\delta = bT/m$ into (24) to get the functions $K_{\text{mmax}}(m)$, $K_{\text{mmax}}(b)$, and $K_{\text{mmax}}(T)$. However, the process is quite complex. In the following we choose δ as the intermediate variable to simplify the analysis.

According to the normalization rule, we can get the following composite functions:

$$K_{\text{mmax}}[\delta(b)] = \frac{m}{T^2}\alpha_{\text{mmax}}, \tag{33}$$

$$K_{\text{mmax}}[\delta(T)] = \frac{b^2}{m}\frac{\alpha_{\text{mmax}}}{\delta^2}, \tag{34}$$

$$K_{\text{mmax}}[\delta(m)] = \frac{b}{T}\frac{\alpha_{\text{mmax}}}{\delta}. \tag{35}$$

Clarifying the influences of $\delta(m)$, $\delta(b)$, and $\delta(T)$ on K_{mmax} can help understand the influences of m, b, and T on K_{mmax} according to the composite function monotonicity determination principles.

The impact of b on K_{mmax} is relatively easy to obtain. Equation (33) shows that the monotonicity of K_{mmax} with respect to δ is the same with that of α_{mmax} to δ. Thus the curve of K_{mmax} to b is with the same shape of α_{mmax} to δ except for the vertical scale by $\frac{m}{T^2}$ and the horizontal scale by $\frac{T}{m}$. The curve when $m = 1$ kg and $T = 0.01$ s is plotted in Fig. 11(a). The variation analysis follows a similar approach as the one presented in Section III-B-I), and thus is omitted here.

Then we will see how T influences K_{mmax}. For (34), through numerical calculations, it is easy to check that

$$\frac{\partial K_{\text{mmax}}}{\partial \delta} \leq 0, \text{ if } \delta \in [0, \infty). \tag{36}$$

Thus, K_{mmax} v.s. δ is a monotonically decreasing function. Consequently, K_{mmax} v.s. T is a monotonically decreasing function. Besides, it is easy to get $K_{\text{mmax}}(0) = \infty$ and $K_{\text{mmax}}(\infty) = 0$. Fig. 11(b) gives the curve of K_{mmax} v.s. T when $b = 10$ Ns/m and $m = 1$ kg. The result shows that reducing the control period T will increase K_{mmax} and thus is an effective way to achieve high VS. However, this will also amplifies the negative impact of other factors, such as the current loop dynamic characteristics, which may limit the mmax-VS. Therefore, reducing T should be cautious.

While the effect of T on K_{mmax} is straightforward, the effect of m on K_{mmax} is more complex. For (35), through numerical calculations, we can find that

$$\frac{\partial K_{\text{mmax}}}{\partial \delta} \begin{cases} \leq 0, & \text{if } \delta \in [0, \delta_{K1}) \cup (\delta_{K2}, \infty), \\ \geq 0, & \text{if } \delta \in (\delta_{K1}, \delta_{K2}), \end{cases} \tag{37}$$

where $\delta_{K1} \approx 1.044$ and $\delta_{K2} \approx 5.775$. Thus, K_{mmax} v.s. δ is a monotonically decreasing function when $\delta \in [0, \delta_{K1}) \cup (\delta_{K2}, \infty)$ and a monotonically increasing function when

$\delta \in (\delta_{K1}, \delta_{K2})$. Consequently, K_{mmax} is a monotonically increasing function with respect to m when $m \in [0, m_{K2}) \cup (m_{K1}, \infty)$ and a monotonically decreasing function when $m \in (m_{K2}, m_{K1})$, where $m_{K2} = \frac{bT}{\delta_{K2}}$ and $m_{K1} = \frac{bT}{\delta_{K1}}$. The local maximum is $K_{\text{mmax}}(m_{K2}) \approx 4.509b/T$, while the local minimum is $K_{\text{mmax}}(m_{K1}) \approx 2.637b/T$. Besides, $K_{\text{mmax}}(0) = 4b/T$ and $K_{\text{mmax}}(\infty) = \infty$. Fig. 11(c) gives the curve of K_{mmax} v.s. m when $b = 10$ Ns/m and $T = 0.01$ s. The result shows that in general, the larger the m the larger the K_{mmax}. But when $m \in (m_{K2}, m_{K1})$, the larger the m the smaller the K_{mmax}.

This can be better understood by referring to Fig. 8(a), which shows the monotonic relationship between the mmax-NVS and the NPD in the normalized parameter space. The non-monotonic behavior in the real parameter space is reflected in the slope of Fig. 8(a), as described below. When the mass m is small (i.e., δ is large), according to the discussions in Section III-B-I), $4\delta + 4$ accurately approximates α_{mmax}. Transformed into the real parameter space, this becomes:

$$\frac{K_{\text{mmax}}T^2}{m} \approx \frac{4bT}{m} + 4, \tag{38}$$

i.e.,

$$K_{\text{mmax}} \approx 4m + 4bT. \tag{39}$$

Therefore, the larger the mass m, the larger the maximum achievable stiffness K_{mmax}. This corresponds to the first increase interval $[0, m_{K2})$. As the mass m increases (i.e., the NPD δ decreases), the curve's slope becomes steeper, and the intercept on the α axis becomes negative. Assume it is:

$$\frac{K_{\text{mmax}}T^2}{m} \approx \frac{l_k bT}{m} - l_b, \tag{40}$$

i.e.,

$$K_{\text{mmax}} \approx -l_b m + l_k bT, \tag{41}$$

where $l_k > 0$ and $l_b > 0$ are the slope and intercept, respectively. Thus, the larger the mass m, the smaller the maximum achievable stiffness K_{mmax}. This corresponds to the decreasing interval (m_{K2}, m_{K1}). As the mass m continues to increase (i.e., the NPD δ decreases), the curve's slope becomes smoother, and the intercept on the α axis becomes positive again. Consequently, the larger the mass m, the larger the maximum achievable stiffness K_{mmax}. This corresponds to the final increasing interval (m_{K1}, ∞). More details on this point are verified by the experiment in Section V-B-III).

B. MMAX-VD AND ITS RELATIONSHIP WITH M, B, AND T

Similar to the last subsection, δ is chosen to be the intermediate variable to simplify the analysis of the influence of m, b, and T on B_{mmax}. According to the normalization rule, we can get the following composite functions:

$$B_{\text{mmax}}[\delta(b)] = \frac{m}{T}\beta_{\text{max}}, \tag{42}$$

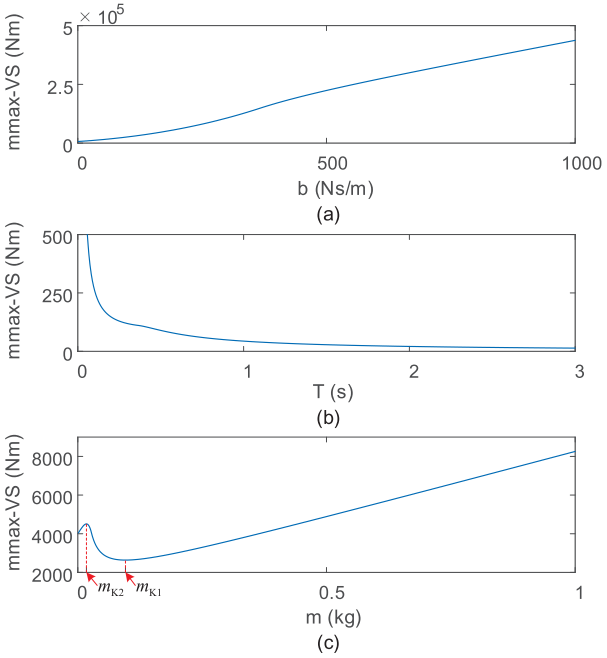

FIGURE 11. K_{mmax} v.s. (a) b when $m = 1$ kg and $T = 0.01$ s, (b) T when $b = 10$ Ns/m and $m = 1$ kg, and (c) m when $b = 10$ Ns/m and $T = 0.01$ s.

$$B_{\text{mmax}}[\delta(T)] = B_{\text{mmax}}[\delta(m)] = b\frac{\beta_{\text{mmax}}}{\delta}. \tag{43}$$

Similar to the analysis of the influence of b on K_{mmax}, the curve of B_{mmax} v.s. b is with the same shape of β_{mmax} v.s. δ except for the vertical scale by $\frac{m}{T}$ and the horizontal scale by $\frac{T}{m}$. The curve when $m = 1$ kg and $T = 0.01$ s is plotted in Fig. 12(a).

Then we will see how T and m influence mmax-VD and mmax-AD. According to Appendix C, $B_{\text{mmax}}(\delta)$ is a monotonically decreasing function in $(0, \delta_B)$ and (δ_0, ∞) and a monotonically increasing function in (δ_B, δ_0) when b is a constant value, where $\delta_B \approx 1.793$. Consequently, the effect of T and m on B_{mmax} can be obtained as shown in Table 1 (in which $T_B = \frac{m}{b}\delta_B$, $T_0 = \frac{m}{b}\delta_0$, $m_0 = \frac{bT}{\delta_0}$, $m_B = \frac{bT}{\delta_B}$). Fig. 12(b) and (c) gives the curves of B_{mmax} v.s. T and m when $b = 10$ Ns/m, $m = 1$ kg and $b = 10$ Ns/m, $T = 0.01$ s, respectively. From Table 1 and Fig. 12 we can see that if the control period T is very large, the system can only add the VD no more than the PD. When T becomes smaller, in general, B_{mmax} increases, except for a short interval $T \in (T_B, T_0)$ where decreasing T decreases B_{mmax}. The influence of m is opposite. If m is very small, the system can only add the VD no more than the PD. When m becomes larger, in general, B_{mmax} increases, except for a short interval $m \in (m_0, m_B)$ where increasing m decreases B_{mmax}. In addition, since b remains constant when analyzing the influences of T and m, the analysis of the mmax-AD v.s. T and m is the same with the mmax-VD v.s. T and m except for a vertical offset b.

In conclusion, we have developed formulas that, for the first time, reveal how the control period, physical damping, and physical inertia influence the mmax-VS and mmax-VD.

TABLE 1. Variations of B_{mmax} along m and T.

–	T or $m \to 0$	1st monotonic interval	Local extremum	2nd monotonic interval	Local extremum	3rd monotonic interval	T or $m \to \infty$
B_{mmax} v.s. T	∞	$(0, T_B)$ ↘	$\approx 3.351b$	(T_B, T_0) ↗	$\approx 3.440b$	(T_0, ∞) ↘	b
B_{mmax} v.s. m	b	$(0, m_0)$ ↗	$\approx 3.440b$	(m_0, m_B) ↘	$\approx 3.351b$	(m_B, ∞) ↗	∞

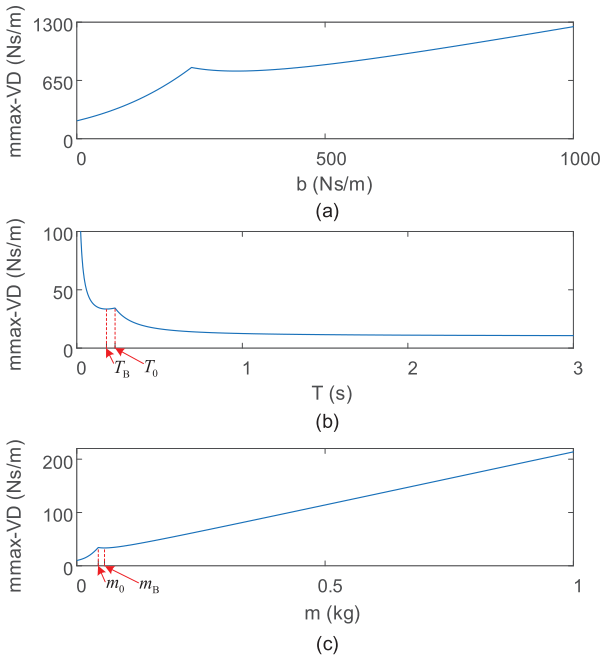

FIGURE 12. B_{mmax} **v.s. (a)** b **when** $m = 1$ **kg and** $T = 0.01$ **s, (b)** T **when** $b = 10$ **Ns/m,** $m = 1$ **kg, and (c)** m **when** $b = 10$ **Ns/m,** $T = 0.01$ **s.**

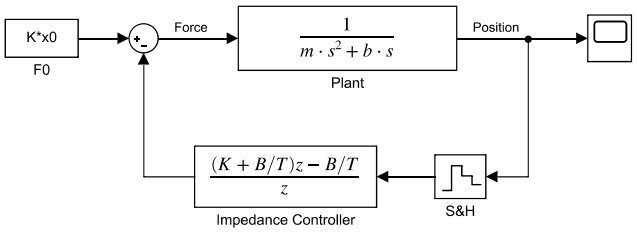

FIGURE 13. Simulation of the impedance-controlled haptic device.

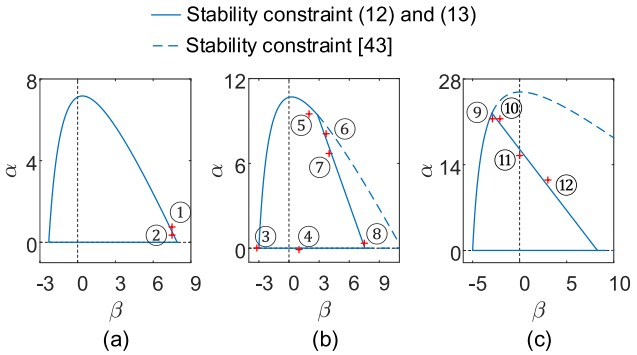

FIGURE 14. Points chosen for the stability boundary verification. (a) $\delta = 2.3$**, (b)** $\delta = 3$**, and (c)** $\delta = 5$**.**

Our findings align with the intuitive expectation of monotonic increasing impacts that reducing the control period and increasing physical damping have on the mmax-VS. However, they also unveil unexpected 'increase-decrease-increase' impacts that increasing physical inertia has on the mmax-VS, and that reducing the control period, increasing physical damping, or increasing physical inertia has on the mmax-VD, challenging traditional views.

V. SIMULATIONS AND EXPERIMENTS

This section will present simulations and experiments to verify the aforementioned theories.

A. SIMULATIONS

The simulation model is shown in Fig. 13, in which $m = 0.1$ kg, $T = 0.01$ s, $b = 23$, 30, and 50 Ns/m representing $\delta = 2.3$, 3, and 5, respectively. The original equilibrium of the virtual stiffness is 0. In order to excite the system, the equilibrium position of the virtual stiffness x_0 is set to 1 m, i.e. the reference force F_0 is set to K. Then if the system is stable, the final position will be 1 m.

Fig. 14 shows the stability boundaries with different δ, in which 12 points are chosen to run the simulation to see the system stability. The chosen point values and the corresponding response results are displayed in Fig. 15. It can be seen that responses of the points inside the stable region are stable and responses of the points outside the stable region are unstable, verifying the stability constraint (12) and (13).

Besides, points 6, 8, 10, and 12 are inside the stable region of the traditional stable constraint [32], [43], but from Fig. 15 we know that the responses of these points are unstable. Thus, the traditional stable constraint as shown in [32] and [43] is only necessary for they do not include the additional linear stability constraint when $\delta > \delta_0$. The stability constraint developed in this article clearly indicates these points are unstable and thus is necessary and sufficient.

What's more, consider the points 2 and 8, which have the same NVD and NVS but with different NPDs. The result that point 2 with smaller NPD is stable but point 8 with larger NPD is unstable indicates that it is not all the case that the larger the NPD, the larger the stability region. As discussed in Section II, this unusual phenomenon happens only if δ is slightly larger than δ_0, in which case the rendered impedance should be carefully considered.

Furthermore, points 5-8 and points 9-12 show that when the NVD reaches a certain threshold, it happens that the larger

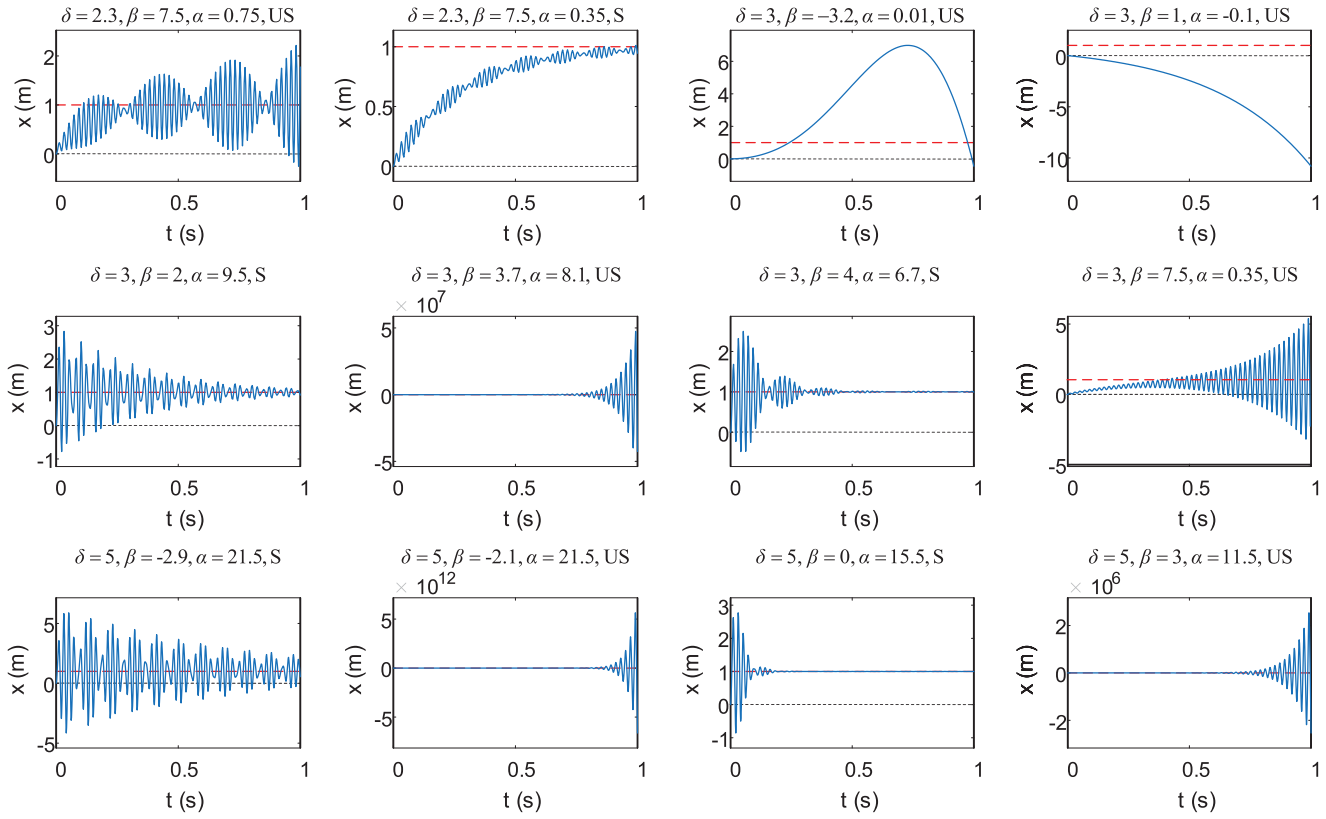

FIGURE 15. Responses of the points chosen in Fig. 14 (S - stable; US - unstable).

the NVD, the smaller the max-NVS. In addition, points 9-12 also indicates that when $\delta > \delta_2$ as long as the NVD is positive, the max-NVS decreases linearly with the increase of the NVD. Thus if one wants to achieve the mmax-NVS, the NVD should be negative. This phenomenon is reported for the first time.

Moreover, the responses of point 3 and point 4 indicate that the system with negative NAS or negative NAD is unstable if there is no interaction with the environment. The comparison of point 9 and point 11 shows that using the NVD item can achieve higher mmax-NVS than the PSC.

B. EXPERIMENTS

Three experiments are implemented to verify the aforementioned theories. The first two verify the stability boundaries in the normalized space when $\delta < \delta_0$ and $\delta > \delta_0$, respectively. The "increase-decrease-increase" pattern in the variation of the mmax-VS along m is presented in the third experiment, verifying the discussions given in Section IV.

The experimental platform is shown in Fig. 16. The controller is TI DRV8301-HC-EVM board attached with microcontroller unit TMS320F28035. The current control period is 25 us for fast current reference ability. Both the drive motor (right) and the load motor (left) are the Maxon EC-4pole 30 PM motors and are connected through a coupling. The characteristics and the differences of the plants

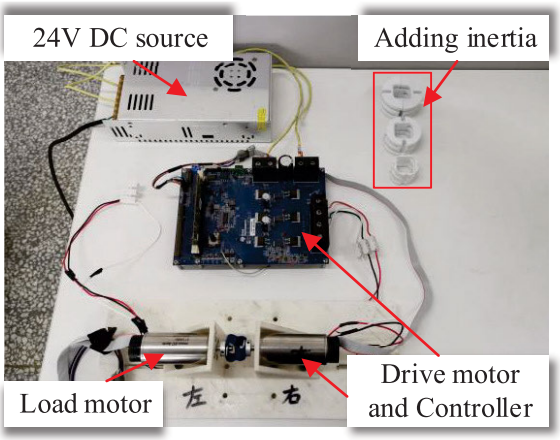

FIGURE 16. Experimental platform.

will be introduced in every experiment. The inertia in the following analysis will be represented by the symbol J.

1) STABILITY BOUNDARY VERIFICATION WHEN NPD $\delta < \delta_0$

Two experiments are implemented to do the verification. The NPD is close to 0 in the first experiment and close to δ_0 in the second.

To make the NPD get close to 0, the load motor keeps open circuit. In fact a single motor would be enough. But

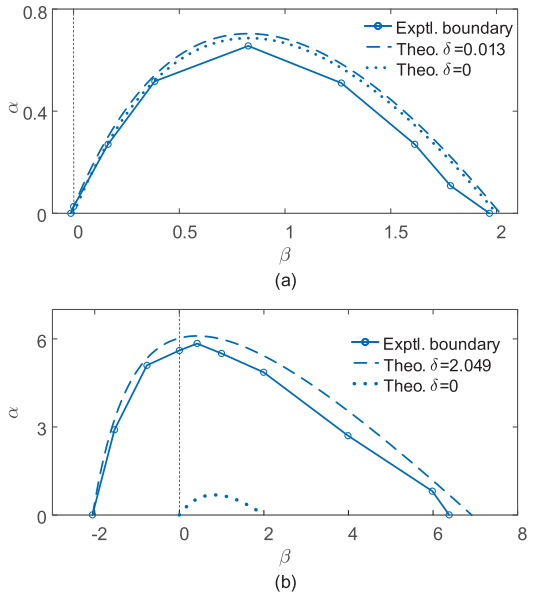

FIGURE 17. Comparison of the experimental and theoretical stability boundaries when $\delta < \delta_0$. (a) $\delta = 0.013$, close to 0. (b) $\delta = 2.049$, close to δ_0.

for the comparison of the following experiments, the same deployment is implemented. In this system, the overall physical damping is identified as $b = 13.93 \times 10^{-6}$ Nms/rad, the inertia is identified as $J = 85.78 \times 10^{-7}$ kgm^2, and the control period is set to be $T = 0.008$ s. Thus, the normalized damping $\delta = 0.013$, close to 0.

To make the NPD get close to δ_0, the load motor's power lines are short-circuited. Since in the load motor, the torque is proportional to the current, the current is proportional to the back electromotive force (back-EMF) and the back-EMF is proportional to the speed, the torque is proportional to the speed. Thus, the load motor provides the driven motor viscous friction. After identification, the physical damping is $b = 2.197 \times 10^{-3}$ Nms/rad, 158 times than the case of open circuit. With the inertia and the control period keeping the same, the normalized damping $\delta = 2.049$, close to δ_0.

During the experiments, a set of constant NVDs including the theoretical NVD to the mmax-NVS are fixed to see the corresponding max-NVSs and at last, set constant NVS $\alpha = 0.001$ to see the corresponding min-NVD (i.e. the approximate mmin-NVD) and max-NVD (i.e. the approximate mmax-NVD). The resulting experimental stability boundaries are transformed to the normalized parameter space and plotted in the solid line in Fig. 17(a) and (b), respectively. In each subfigure, the dashed line displays the theoretical stability boundary of the corresponding δ.

According to Fig. 17, we can see that the experimental stability boundaries match the theoretical boundaries very well under both cases, thus indicating the accuracy of the theory.

For comparison, the theoretical boundary when $\delta = 0$ is also plotted in Fig. 17(a) and (b) in the dotted line. It is close to the theoretical and experimental stability boundaries for the case where δ approaches 0, as shown in Fig. 17(a). Thus we can use the stability boundary of $\delta = 0$ to approximate that of small δ. But when δ is much larger than 0, as shown in Fig. 17(b), the difference are very large. In this case, the approximation is no longer held. Both experimental results verify the discussions given in Section II-D.

By comparing Fig. 17(a) and (b), it is evident that increasing the NPD leads to a considerable expansion of the stability region in the normalized parameter space. Since the control period and the inertia are the same in both cases, the results also indicate that increasing the physical damping generally results in a larger stability region in the real parameter space. In practice, there are kinds of methods increasing the physical damping of the system to render larger impedance [50], [51], [52], [53].

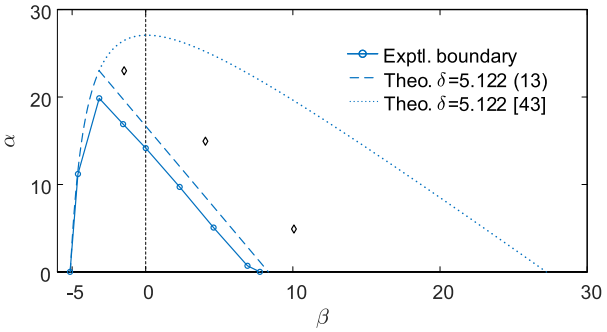

FIGURE 18. Comparison of the experimental and theoretical stability boundaries when $\delta = 5.122 > \delta_0$.

2) STABILITY BOUNDARY VERIFICATION WHEN NPD $\delta > \delta_0$

Set the control period of the deployment with the load motor short-circuited to $T = 0.02$ s, then the NPD is $\delta = 5.122$, which is larger than δ_0. The resulting experimental stability boundary in the normalized parameter space is plotted as the solid line in Fig. 18. The dashed line displays the theoretical stability boundary when $\delta = 5.122$. It can be seen that the experimental stability boundary matches the theoretical boundary very well, thus indicating the accuracy of the theory when $\delta > \delta_0$.

For comparison, the theoretical boundary of work [43] (i.e. the stability constraint without the linear constraint when $\delta > \delta_0$) is also plotted in the same figure in dotted line. Three points, as indicated by the diamond mark, are chosen to see the experimental responses. They locate far inside the stability boundary of work [43] but beyond the theoretical boundary in this article. The experimental responses of all these three points are unstable even with a step of only 5° in angular position, as shown in Fig. 19. This implies that points inside the theoretical stability boundary of [43] could be unstable, indicating the inaccuracy of the theoretical stability boundary of [43] when $\delta > \delta_0$. This is because it does not consider the linear constraint when $\delta > \delta_0$.

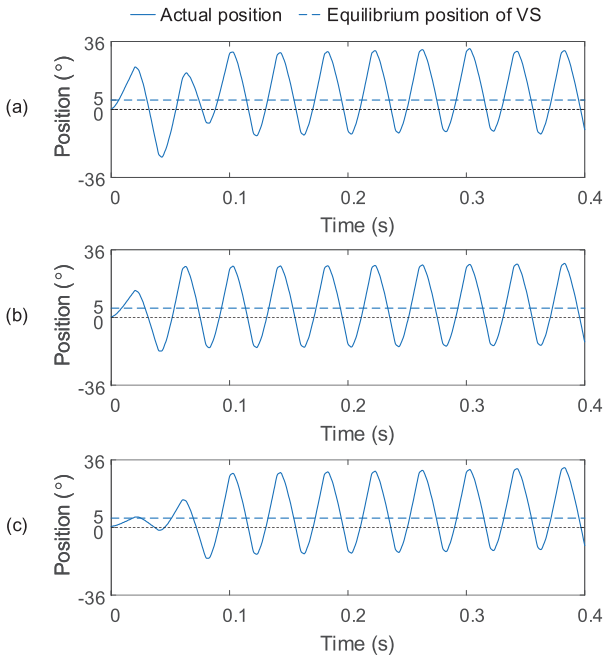

FIGURE 19. Experimental responses of the three points diamond marked in Fig. 18. (a) $\beta = -1.5, \alpha = 23$. (b) $\beta = 4, \alpha = 15$. (c) $\beta = 10, \alpha = 5$.

TABLE 2. Comparison of the experimental max-NVSs of PSC and the experimental mmax-NVSs.

δ	$\alpha_{\max}$ of PSC	α_{mmax}	$\beta_{\alpha_{\text{mmax}}}$	$\delta + \beta_{\alpha_{\text{mmax}}}$	Increase factor
0.013	0.026	0.656	0.826	0.839	24.837
2.049	5.611	5.847	0.421	2.470	1.042
5.122	14.154	19.858	−3.162	1.960	1.403

Besides, comparing the max-NVSs of PSC and the mmax-NVSs of all the above three cases in Table 2, we can see that comparing to PSC, adding the item of the NVD can increase the mmax-NVS the system can render. When $\delta = 0.013$, the mmax-NVS increases by a factor of up to 24.837 times. Furthermore, it can also be seen that when $\delta < \delta_2$ positive NVD leads to the mmax-NVS while when $\delta > \delta_2$ negative NVD leads to the mmax-NVS. In addition, the differences of NADs are not that much as NVDs. These observations verify the discussions in Section III-B-I).

Moreover, comparing the experimental stability boundaries of the case $\delta = 2.049$ and the case $\delta = 5.122$ in the normalized parameter space in Fig. 20(a), we can see that the case $\delta = 5.122$ has a wider stability region. Then, as m and b are the same for both cases, it seems to suggest that the larger the T the larger the stability region. However, if we compare their stability boundaries in the real parameter space, as shown in Fig. 20(b), we can see that the case $\delta = 5.122$ actually has a narrower stability region. This is different from the situation mentioned in Section V-B-I), where increasing b enlarges both the stability region in the normalized parameter space and the stability region in the real parameter space. Therefore, although both can lead to an

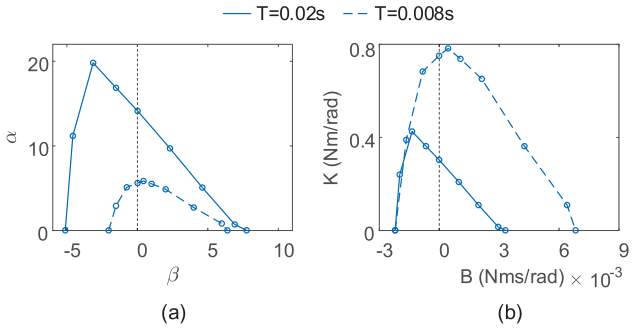

FIGURE 20. Comparison of the stability region when T is different in (a) the normalized parameter space and (b) the real parameter space.

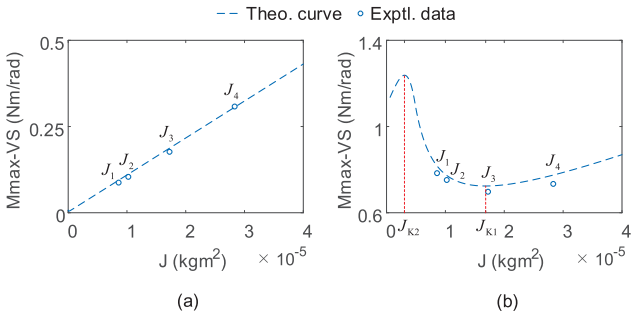

FIGURE 21. Influence of the inertia on the mmax-VS. (a) The load motor is open circuit. (b) The load motor is short-circuited.

expansion of δ and thus the stability region in the normalized parameter space, increasing T reduces the stability region in the real parameter space, while increasing b, on the contrary, results in an expansion of the stability region in the real parameter space. This can be perplexing for many. Since the relationships of the real parameters are the ultimate concern, we have to explore the stability region variations in the real parameter space, as discussed in Section IV and experimentally verified in the next subsection.

3) INFLUENCE OF THE INERTIA ON MMAX-VS

In order to verify the influence of the inertia on the mmax-VS, we add extra inertia on the coupling. By doing so, the inertia changed to $J_2 = 102.29 \times 10^{-7}$ kgm^2, $J_3 = 172.43 \times 10^{-7}$ kgm^2, and $J_4 = 283.21 \times 10^{-7}$ kgm^2. Both cases where the load motor is open circuit and short-circuited are experimented with these three new inertia. The control period $T = 0.008$ s. Set the constant NVD to the corresponding $\beta_{\alpha_{\text{mmax}}}$ to see the mmax-NVS. The results, together with the mmax-VSs obtained in Experiment 1) ($J_1 = 85.78 \times 10^{-7}$ kgm^2), are plotted in real units in Fig. 21.

From Fig. 21, it can be seen that the influence of the physical inertia on the mmax-VS is not simply monotonically increasing or decreasing. When the load motor is open circuit, as the inertia is much larger than $J_{K1} = 1.07 \times 10^{-7}$ kgm^2, the mmax-VS is larger when the inertia is larger. However, when the load motor is short-circuited, the variation exhibits an ''increase-decrease-increase'' pattern. For clarity, critical

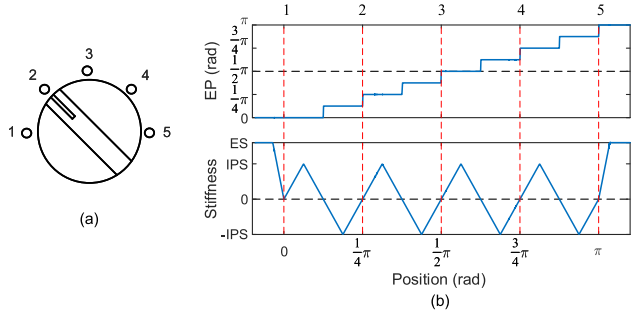

FIGURE 22. Illustration of (a) the emulated five-position knob switch and (b) the virtual stiffness and equilibrium position (EP) planning used for its implementation.

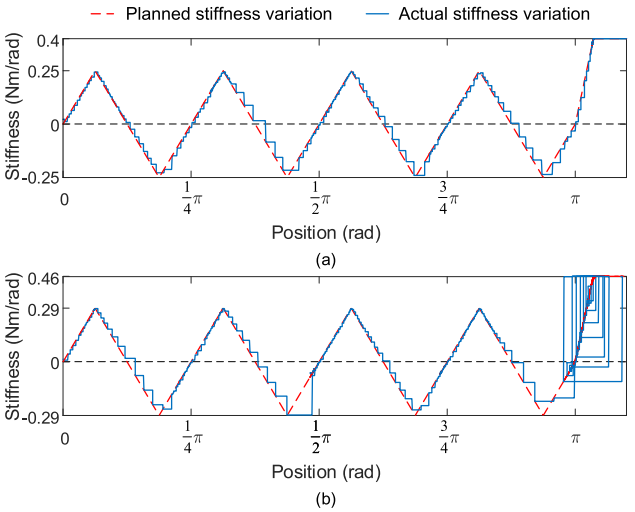

FIGURE 23. Comparison of planned and actual stiffness variations during the clockwise rotation of the virtual knob switch, with stiffness planned based on (a) proposed stability constraint and (b) existing stability constraint [43].

inertia $J_{K2} = 30.43 \times 10^{-7}$ kgm^2 and $J_{K1} = 168.40 \times 10^{-7}$ kgm^2 are also marked in the figure. It can be seen from the figure that even though the inertia J_2 is larger than J_1, the mmax-VS is lower. The situation of J_3 to J_2 is the same. It is because these inertia are in the decreasing interval (J_{K2}, J_{K1}). Afterwards when the inertia becomes larger to J_4, the mmax-VS is higher since the inertia is in the increasing interval (J_{K1}, ∞). This verifies the discussion in Section IV that K_{mmax} v.s. J is a monotonically increasing function when $J \in [0, J_{K2}) \cup (J_{K1}, \infty)$ and a monotonically decreasing function when $J \in (J_{K2}, J_{K1})$.

4) GENERALITY TEST: VARIABLE IMPEDANCE VIRTUAL KNOB SWITCH

In the following variable impedance control experiment, we emulate a five-position knob switch to demonstrate the generality and practical applicability of our theoretical findings.

The multi-position knob switch, known for its widespread use and user-friendly design, enables effortless management of state transitions in devices or systems. We emulate a five-position knob switch, as depicted in Fig. 22(a), through a straightforward virtual spring mechanism (Fig. 22(b)). Each switch position is flanked by positive and negative stiffnesses, providing users with clear, detent tactile feedback. Additionally, virtual walls are established at both ends of the range, restricting the knob's rotation.

In the emulation endeavor, the deployment with the load motor short-circuited and $T = 0.02$ s, is employed. This is necessitated by the inadequacies found in the deployment with the load motor open-circuited, which only allows for a mmax-VS of 0.0874 Nm/rad, equating to a torque of merely 0.0172 Nm at $\pi/16$ rad. Such capability falls short of producing clearly distinguishable switch sensations. Given the NPD now is $\delta = 5.122$, exceeding θ_0 as highlighted in Section II, the stability constraint derived from existing theories [32], [43] becomes inapplicable. This is attributed to their suggestion of an overly wide stiffness range, potentially leading to instability and creating safety hazards. In contrast, our proposed theoretical framework is capable of offering an accurate stiffness range for all NPDs including such a scenario.

The mmax-VS for this deployment is 0.49 Nm/rad, obtained by setting the VD to -1.36×10^{-3} Nms/rad, as detailed in Section III. Accordingly, we set the end stiffness (ES) at 0.4 Nm/rad (approximately 80% of the mmax-VS) and the intermediate peak stiffness (IPS) at 0.25 Nm/rad (approximately 50% of the mmax-VS) to emulate the tactile sensation of a physical knob switch. Rotating the virtual knob switch clockwise from Position 1 yields the actual stiffness variation shown in Fig. 23(a). The results affirm that the system is stable and aligns with the design objectives. For comparison, another emulation of the virtual knob switch is conducted based on the existing stability constraint [43]. The settings for this emulation are: 0.58 Nm/rad for mmax-VS, 0.03×10^{-3} Nms/rad for the VD to achieve mmax-VS, 0.46 Nm/rad for ES, and 0.29 Nm/rad for IPS. The planned and actual stiffness variations corresponding to these settings are presented in Fig. 23(b). The figure reveals that while the system is stable and follows the planned stiffness variation during the intermediate process, the interaction with the virtual wall exhibits oscillatory behavior. This result is attributed to the ES designed based on [43] exceeding the stability boundary of this deployment.

Furthermore, based on the analysis in Section IV, the mmax-VS for this deployment can be increased by reducing the control period, increasing the physical damping, or decreasing the physical inertia to $J'_{K2} = 76.09 \times 10^{-7}$ kgm^2. While the first two methods are well-known to researchers, the third one presents a novel approach, challenging the traditional belief that higher inertia leads to greater mmax-VS [46]. This recommendation emerges from the observation that the current inertia lies within the "decrease" phase of the "increase-decrease-increase"

pattern, indicating an increase in mmax-VS through inertia reduction. The optimal result is obtained by decreasing the inertia to J'_{K2}, as further reduction negatively impacts the mmax-VS. On the flip side, while it is technically possible to increase the inertia for a higher mmax-VS, such an increment should reach at least 1943×10^{-7} kgm^2, at which point the mmax-VS is equivalent to that of J'_{K2}. However, since this increase amplifies J'_{K2} by twenty-sixfold, the benefits do not justify the drawbacks. Therefore, reducing the inertia to J'_{K2} is identified as the preferred approach.

VI. CONCLUSION AND FUTURE WORK

This paper presents the complete analytical uncoupled stability constraint for impedance-controlled haptic devices in the normalized parameter space. Unlike the existing constraint, which may lead to instability when $\delta > \delta_0$, the proposed constraint is applicable for all NPDs. The uniqueness is the revealing of a linear constraint when $\delta > \delta_0$ so that unstable points can be excluded. This noticeable discovery also brings in new insights. Though in general the larger the NPD the larger the stability region, there are exceptional cases where enlarging the NPD might lead to instability. This happens when δ is slightly larger than δ_0. Besides, adding positive NVD does not necessarily result in higher max-NVS. When $\delta > \delta_2$, the mmax-NVS occurs at negative NVD.

Furthermore, this study delves deeper into the real parameter space to examine the impacts of physical parameters on achievable impedance extremes. This is crucial because our primary focus is on drawing accurate conclusions in the real parameter space, which has been lacking in existing analyses or experiments. For the first time, we derive formulas for the mmax-VS and mmax-VD as functions of control period, physical damping, and physical inertia. It is shown that while it is intuitive that reducing the control period and increasing the physical damping will enlarge the mmax-VS, the other four contradict with the traditional impressions. Specifically, increasing the physical inertia will lead to an "increase-decrease-increase" pattern of the mmax-VS. Similarly, reducing the control period, increasing the physical damping or the physical inertia will lead to an "increase-decrease-increase" pattern of the mmax-VD. With the accurate uncoupled stability constraint and influence curves of physical parameters on achievable impedance extremes, the proposed approach serves as a crucial basis for the stability analysis and controller design of practical haptic interaction systems, ensuring safe physical human-robot interaction.

Future research related to the framework of the uncoupled stability will take other factors such as the characteristics of the current loop, the velocity filter, the encoder resolution, and the Coulomb friction into account. The theoretical requirement of the environment that ensures the stability of the overall system when interacting with a stable device is also worthy to be investigated.

APPENDIX A
DERIVATION OF PROPERTIES OF $C_{\delta 1}(\delta)$ AND $C_{\delta 2}(\delta)$

This appendix derives several properties of the intermediate functions $c_{\delta 1}(\delta)$ and $c_{\delta 2}(\delta)$, as defined in (3) and (4), respectively. Both of them are monotonically decreasing functions and in the range $(0, 1]$ when $\delta \in [0, \infty)$. Besides, $c_{\delta 1}(\delta) \geq c_{\delta 2}(\delta)$ and "=" is true if and only if $\delta = 0$.

A. BOTH $C_{\delta 1}(\delta)$ AND $C_{\delta 2}(\delta)$ ARE MONOTONICALLY DECREASING FUNCTIONS AND IN RANGE $(0, 1]$

When $\delta \in (0, \infty)$, the derivative function of $c_{\delta 1}(\delta)$ is

$$c'_{\delta 1}(\delta) = \frac{-(\delta+2)e^{-\delta} - (\delta-2)}{\frac{\delta^3}{2}}. \tag{44}$$

Let

$$h_1(\delta) = -(\delta+2)e^{-\delta} - (\delta-2), \tag{45}$$

then its first and second derivative functions are

$$h'_1(\delta) = (\delta+1)e^{-\delta} - 1, \tag{46}$$

$$h''_1(\delta) = -\delta e^{-\delta}. \tag{47}$$

Since $h''_1(\delta) < 0$ when $\delta \in (0, \infty)$, the following inequalities can be obtained successively:

$$h'_1(\delta) < h'_1(0) = 0, \tag{48}$$

$$h_1(\delta) < h_1(0) = 0, \tag{49}$$

$$c'_{\delta 1}(\delta) < 0. \tag{50}$$

Thus, $c_{\delta 1}(\delta)$ is a monotonically decreasing function when $\delta \in (0, \infty)$ and

$$0 = c_{\delta 1}(\infty) < c_{\delta 1}(\delta) < c_{\delta 1}(0) = 1. \tag{51}$$

Therefore, considering that $c_{\delta 1}(\delta) = 1$ when $\delta = 0$, the proof of the properties of $c_{\delta 1}(\delta)$ is completed.

Similarly, we find that $c_{\delta 2}(\delta)$ is also a monotonically decreasing function and in the range $(0, 1]$ when $\delta \in [0, \infty)$.

B. $C_{\delta 1}(\delta) \geq C_{\delta 2}(\delta)$ AND "=" IS TRUE IF AND ONLY IF $\delta = 0$

When $\delta \in (0, \infty)$, the difference of these two functions is

$$c_{\delta 1}(\delta) - c_{\delta 2}(\delta) = \frac{(\delta+2)e^{-\delta} + (\delta-2)}{\frac{\delta^2}{2}}. \tag{52}$$

From (49), we know that

$$(\delta+2)e^{-\delta} + (\delta-2) > 0. \tag{53}$$

Thus, when $\delta \in (0, \infty)$,

$$c_{\delta 1}(\delta) > c_{\delta 2}(\delta). \tag{54}$$

Therefore, considering that $c_{\delta 1}(\delta) = c_{\delta 2}(\delta) = 1$ when $\delta = 0$, the proof is completed.

APPENDIX B
DERIVATION OF STABILITY CONSTRAINT

This appendix derives the explicit stability constraint (10) and the more detailed cases (12) and (13). Since the case $\delta = 0$ can be easily verified, we will assume $\delta \neq 0$ in the following.

A. INTERSECTION AREA CONSTRAINED BY FIRST THREE INEQUALITIES OF (9)

Substituting 1 and -1 into the denominator polynomial (7), we can get

$$\begin{aligned} p_d(1) &= (c_{\delta 1} + c_{\delta 2})\alpha \\ p_d(-1) &= (c_{\delta 1} - c_{\delta 2})(\alpha + 2\beta) - 4(1 + e^{-\delta}). \end{aligned} \tag{55}$$

As derived in Appendix A, $c_{\delta 1} > 0$, $c_{\delta 2} > 0$, and $c_{\delta 1} > c_{\delta 2}$ when $\delta > 0$, thus the first three inequalities of (9) simplify to

$$\begin{cases} \alpha & > 0 \\ \alpha + 2\beta & < \dfrac{4(1 + e^{-\delta})}{c_{\delta 1} - c_{\delta 2}} \\ |\beta| & < \dfrac{2}{c_{\delta 2}} \end{cases}. \tag{56}$$

It is easy to verify that, without considering the inequality $\beta < \frac{2}{c_{\delta 2}}$, constraint (56) bounded a triangular area in the $\beta - \alpha$ plane. Since the vertical line $\beta = \frac{2}{c_{\delta 2}}$ could be to the right of the triangular area or could intersect it, the constraint (56) can be further divided into two cases.

For clarity, the upper boundary line of the area constrained by the second inequality is denoted by l_1. The intersection point of l_1 and the horizontal β axis, i.e. the right vertex of the triangle, is $(\frac{2(1+e^{-\delta})}{c_{\delta 1} - c_{\delta 2}}, 0)$. Assuming the vertical line $\beta = \frac{2}{c_{\delta 2}}$ is to the right of the triangular area, we have

$$\frac{2(1 + e^{-\delta})}{c_{\delta 1} - c_{\delta 2}} < \frac{2}{c_{\delta 2}}. \tag{57}$$

It can be simplified to

$$(1 + \delta)\left(1 + e^{-\delta}\right)^2 > 4. \tag{58}$$

The exact solution of the inequality is difficult to obtain, but a numerical solution can be acquired. It is $\delta > \delta_0$, where $\delta_0 \approx 2.311$. Hence, (56) can be divided into the following two cases:

1) if $\delta \le \delta_0$

$$\begin{cases} \alpha & > 0 \\ -\dfrac{2}{c_{\delta 2}} < \beta & < \min\left\{\dfrac{2}{c_{\delta 2}}, \dfrac{2(1 + e^{-\delta})}{c_{\delta 1} - c_{\delta 2}} - \dfrac{\alpha}{2}\right\} \end{cases}, \tag{59}$$

2) if $\delta > \delta_0$

$$\begin{cases} \alpha & > 0 \\ -\dfrac{2}{c_{\delta 2}} < \beta & < \dfrac{2(1 + e^{-\delta})}{c_{\delta 1} - c_{\delta 2}} - \dfrac{\alpha}{2} \end{cases} \tag{60}$$

indicating a trapezoidal area and a triangular area, respectively. Fig. 24 shows the resulted intersection areas for both cases.

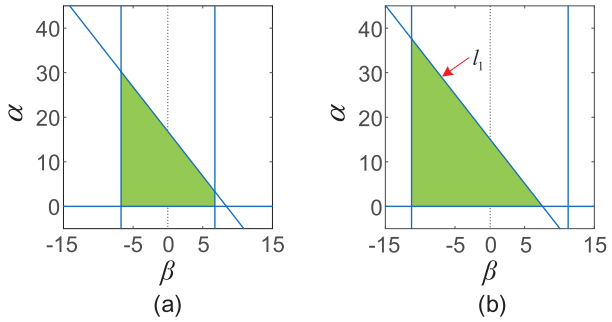

FIGURE 24. Intersection area constrained by the first three inequalities of (9). (a) $\delta = 2 \le \delta_0$, (b) $\delta = 3 > \delta_0$.

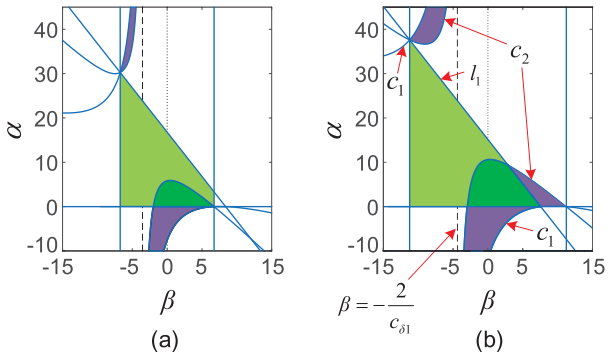

FIGURE 25. Intersection area constrained by all the four inequalities of (9). (a) $\delta = 2 \le \delta_0$, (b) $\delta = 3 > \delta_0$.

B. SIMPLIFICATION OF THE FOURTH INEQUALITY OF (9)

The fourth inequality of (9) can be changed to the intersection of the inequalities

$$\begin{aligned} &(c_{\delta 1} - c_{\delta 2})c_{\delta 2}\beta^2 + c_{\delta 1}c_{\delta 2}\alpha\beta \\ &\quad + 2c_{\delta 2}\alpha - 2(c_{\delta 1} + e^{-\delta}c_{\delta 2})\beta + 4(1 + e^{-\delta}) > 0 \end{aligned} \tag{61}$$

and

$$\begin{aligned} &(c_{\delta 1} + c_{\delta 2})c_{\delta 2}\beta^2 + c_{\delta 1}c_{\delta 2}\alpha\beta \\ &\quad + 2c_{\delta 2}\alpha - 2(c_{\delta 1} + e^{-\delta}c_{\delta 2})\beta - 4(1 - e^{-\delta}) < 0. \end{aligned} \tag{62}$$

The symbols c_1 and c_2 are used to represent the boundary curves of (61) and (62), respectively. It is worth noting that both c_1 and c_2 are second-order curves. Therefore, their shapes and positions can be determined based on the second-order curve theory. After calculations, it is found that they are hyperbolas with centers in the second quadrant. Additionally, for both of them, the slope of the real axis is negative and the slope of the imaginary axis is positive. The resulted shapes and positions of c_1 and c_2 are shown in Fig. 25.

Besides, since no solution exists when substituting $\beta = -\frac{2}{c_{\delta 1}}$ into either c_1 or c_2, the branches of both c_1 and c_2 are separated by the vertical line $\beta = -\frac{2}{c_{\delta 1}}$. Then with $f(\beta)$ defined in (11) and

$$g(\beta) = \frac{-(c_{\delta 1} - c_{\delta 2})c_{\delta 2}\beta^2 + 2(c_{\delta 1} + e^{-\delta}c_{\delta 2})\beta - 4(1 + e^{-\delta})}{(c_{\delta 1}\beta + 2)c_{\delta 2}}, \tag{63}$$

the intersection of inequalities (61) and (62) can be simplified to

$$\begin{cases} g(\beta) < \alpha < f(\beta), & \text{if } \beta > -\dfrac{2}{c_{\delta 1}}, \\ f(\beta) < \alpha < g(\beta), & \text{if } \beta < -\dfrac{2}{c_{\delta 1}}. \end{cases} \tag{64}$$

The purple shadow regions in Fig. 25 illustrate this.

What's more, taking the result of the last subsection into account, constraint (64) can be further simplified.

1) THE SECOND CASE OF (64) IS DISCARDED

Combining the equations of l_1 and c_2, we can get their intersection points:

$$\left(-\frac{2}{c_{\delta 2}}, \frac{4(c_{\delta 1}+e^{-\delta}c_{\delta 2})}{c_{\delta 2}(c_{\delta 1}-c_{\delta 2})}\right) \tag{65}$$

and

$$\left(\frac{2[(3+e^{-\delta})c_{\delta 2}-(1-e^{-\delta})c_{\delta 1}]}{(c_{\delta 1}-c_{\delta 2})^2}, \frac{8[c_{\delta 1}-(2+e^{-\delta})c_{\delta 2}]}{(c_{\delta 1}-c_{\delta 2})^2}\right). \tag{66}$$

It is easy to check that

$$-\frac{2}{c_{\delta 2}} < -\frac{2}{c_{\delta 1}} \tag{67}$$

and

$$\frac{2[(3+e^{-\delta})c_{\delta 2}-(1-e^{-\delta})c_{\delta 1}]}{(c_{\delta 1}-c_{\delta 2})^2} > -\frac{2}{c_{\delta 1}}. \tag{68}$$

Thus the intersection points are located in the left branch and right branch of c_2, respectively. Then for points with $\beta \in \left(-\frac{2}{c_{\delta 2}}, -\frac{2}{c_{\delta 1}}\right)$, the requirements to be under l_1 and above c_2 are in conflict, as shown in Fig. 25. Therefore, the second case of (64) has no intersection with the area constrained by (56) and thus is discarded.

2) SIMPLIFICATION OF THE FIRST CASE OF (64)

By setting $\alpha = 0$ in (61), we can get the intersection points of c_1 and the β axis: $\left(\frac{2}{c_{\delta 2}}, 0\right)$ and $\left(\frac{2(1+e^{-\delta})}{c_{\delta 1}-c_{\delta 2}}, 0\right)$. Then for points with $\beta \in \left(-\frac{2}{c_{\delta 1}}, \min\left\{\frac{2}{c_{\delta 2}}, \frac{2(1+e^{-\delta})}{c_{\delta 1}-c_{\delta 2}}\right\}\right)$, $g(\beta) < 0$. Therefore, the left inequality $\alpha > g(\beta)$ in the first case of (64) is redundant to the first inequality $\alpha > 0$ in (56).

In addition, by setting $\alpha = 0$ in (62), we can get the intersection points of c_2 and the β axis: $(-\delta, 0)$ and $\left(\frac{2}{c_{\delta 2}}, 0\right)$. Then for a point satisfying both $\alpha > 0$ and $\alpha < f(\beta)$, its β coordinate is in $\left(-\delta, \frac{2}{c_{\delta 2}}\right)$. Hence, the condition $\beta > -\frac{2}{c_{\delta 1}}$ in the first case of (64) can be replaced by $\beta > -\delta$.

To conclude, taking the result of Appendix B-A into account, the fourth inequality of (9) can be simplified to

$$\beta > -\delta \text{ and } \alpha < f(\beta). \tag{69}$$

C. EXPLICIT STABILITY CONSTRAINT OF THE SYSTEM

While the result in Appendix B-A help simplify the fourth inequality of (9) in the last subsection, the simplified fourth inequality (69) can, in turn, simplify the result in Appendix B-A and derive the explicit stability constraint of the system.

From the last subsection, we know that for a point satisfying (69), its β coordinate is in $\left(-\delta, \frac{2}{c_{\delta 2}}\right)$. Thus it is in $(-\frac{2}{c_{\delta 2}}, \frac{2}{c_{\delta 2}})$. Therefore, the third inequality of (56) is redundant. Consequently, the stability constraint (10) is acquired.

Furthermore, it is easy to check that when $\delta \le \delta_0$, the only intersection point of l_1 and the right branch of c_2 (i.e. the point (66)) is at the right-down position to the point $\left(\frac{2}{c_{\delta 2}}, 0\right)$, which is the right intersection point of the right branch of c_2 and the β axis. Thus the line l_1 is above the right branch of c_2 when $\alpha > 0$. Therefore, the second inequality of (56) is redundant when $\delta \le \delta_0$. Consequently, two detailed cases of the system stability constraint (12) and (13) are acquired. The dark green shadow regions in Fig. 25 illustrate this.

APPENDIX C
DERIVATIONS IN SECTION IV-B

This appendix analyzes the monotonicity of B_{mmax} v.s. δ when b is a constant value.

1) If $\delta \le \delta_0$

$$B'_{\text{mmax}}(\delta) = b\frac{1-e^{-\delta}-\delta e^{-\delta}-\delta^2 e^{-\delta}}{(1-e^{-\delta}-\delta e^{-\delta})^2}. \tag{70}$$

Let

$$g_1(\delta) = 1-e^{-\delta}-\delta e^{-\delta}-\delta^2 e^{-\delta}, \tag{71}$$

then its derivative function is

$$g'_1(\delta) = \delta(\delta-1)e^{-\delta}. \tag{72}$$

Thus,

$$g'_1(\delta)\begin{cases} < 0, & \text{if } \delta \in (0,1), \\ > 0, & \text{if } \delta \in (1,\infty). \end{cases} \tag{73}$$

Therefore, $g_1(\delta)$ is monotonically decreasing in $(0, 1)$ and monotonically increasing in $(1, \infty)$. Since $g_1(0) = 0$, $g_1(\infty) = 1$, there is another zero in $(0, \infty)$. Through numerical calculations, we can obtain the zero to be $\delta_B \approx 1.793$. Consequently,

$$B'_{\text{mmax}}(\delta)\begin{cases} < 0, & \text{if } \delta \in (0,\delta_B), \\ > 0, & \text{if } \delta \in (\delta_B,\delta_0). \end{cases} \tag{74}$$

Hence, $B_{\text{mmax}}(\delta)$ is a monotonically decreasing function for $\delta \in (0, \delta_B)$ and a monotonically increasing function for $\delta \in (\delta_B, \delta_0)$. The minimum value is $B_{min}(\delta_B) \approx 3.351b$.

2) If $\delta > \delta_0$

$$B'_{\text{mmax}}(\delta) = -2b\frac{1-2\delta e^{-\delta}-e^{-2\delta}}{[(\delta-2)+(\delta+2)e^{-\delta}]^2}. \tag{75}$$

Let

$$g_2(\delta) = 1 - 2\delta e^{-\delta} - e^{-2\delta}, \tag{76}$$

then its derivative function is

$$g_2'(\delta) = 2(-1 + \delta + e^{-\delta})e^{-\delta}. \tag{77}$$

Since $g_2'(\delta) > 0$ when $\delta \in (0, \infty)$, we can know

$$g_2(\delta) > g_2(0) = 0. \tag{78}$$

Thus,

$$B'_{\text{mmax}} < 0, \text{if } \delta > \delta_0. \tag{79}$$

Therefore, $B_{\text{mmax}}(\delta)$ is a monotonically decreasing function when $\delta > \delta_0$ and

$$B_{\text{mmax}}(\delta) > B_{\text{mmax}}(\delta_0) \approx 3.440b \tag{80}$$

In summary, when b is a constant value, B_{mmax} is a monotonically decreasing function in $(0, \delta_B)$ and (δ_0, ∞) and a monotonically increasing function in (δ_B, δ_0). The local minimum is $B_{\text{mmax}}(\delta_B) \approx 3.351b$, while the local maximum is $B_{\text{mmax}}(\delta_0) \approx 3.440b$. In addition, $B_{\text{mmax}}(0) = \infty$ and $B_{\text{mmax}}(\infty) = b$.

REFERENCES

[1] A. Gupta and M. K. O'Malley, "Design of a haptic arm exoskeleton for training and rehabilitation," *IEEE/ASME Trans. Mechatronics*, vol. 11, no. 3, pp. 280–289, Jun. 2006.

[2] M.-A. Choukou, S. Mbabaali, J. Bani Hani, and C. Cooke, "Haptic-enabled hand rehabilitation in stroke patients: A scoping review," *Appl. Sci.*, vol. 11, no. 8, p. 3712, Apr. 2021.

[3] A. M. Okamura, "Haptic feedback in robot-assisted minimally invasive surgery," *Current Opinion Urol.*, vol. 19, no. 1, pp. 102–107, Jan. 2009.

[4] N. Enayati, E. De Momi, and G. Ferrigno, "Haptics in robot-assisted surgery: Challenges and benefits," *IEEE Rev. Biomed. Eng.*, vol. 9, pp. 49–65, 2016.

[5] S. L. Bolding and U. N. Reebye, "Accuracy of haptic robotic guidance of dental implant surgery for completely edentulous arches," *J. Prosthetic Dentistry*, vol. 128, no. 4, pp. 639–647, Oct. 2022.

[6] G. Hirzinger, K. Landzettel, and D. Reintsema, "ROKVISS-Robotics component verification on ISS," in *Proc. Int. Symp. Artif. Intell., Robot. Autom. Space (iSAIRAS)*, 2005, p. 132.

[7] M. Panzirsch, A. Pereira, H. Singh, B. Weber, and E. Ferreira, "Exploring planet geology through force-feedback telemanipulation from orbit," *Sci. Robot.*, vol. 7, no. 65, Apr. 2022, Art. no. eabl6307.

[8] S. M. Petermeijer, D. A. Abbink, M. Mulder, and J. C. F. de Winter, "The effect of haptic support systems on driver performance: A literature survey," *IEEE Trans. Haptics*, vol. 8, no. 4, pp. 467–479, Oct. 2015.

[9] Z. Wang, R. Zheng, T. Kaizuka, K. Shimono, and K. Nakano, "The effect of a haptic guidance steering system on fatigue-related driver behavior," *IEEE Trans. Hum.-Mach. Syst.*, vol. 47, no. 5, pp. 741–748, Oct. 2017.

[10] C. Wang, F. Li, Y. Wang, and J. R. Wagner, "Haptic assistive control with learning-based driver intent recognition for semi-autonomous vehicles," *IEEE Trans. Intell. Vehicles*, vol. 8, no. 1, pp. 425–437, Jan. 2023.

[11] D. Van Baelen, M. M. van Paassen, J. Ellerbroek, D. A. Abbink, and M. Mulder, "Flying by feeling: Communicating flight envelope protection through haptic feedback," *Int. J. Hum.-Comput. Interact.*, vol. 37, no. 7, pp. 655–665, Apr. 2021.

[12] A. F. Abate, M. Guida, P. Leoncini, M. Nappi, and S. Ricciardi, "A haptic-based approach to virtual training for aerospace industry," *J. Vis. Lang. Comput.*, vol. 20, no. 5, pp. 318–325, Oct. 2009.

[13] C. F. Mackenzie, T. E. Harris, A. G. Shipper, E. Elster, and M. W. Bowyer, "Virtual reality and haptic interfaces for civilian and military open trauma surgery training: A systematic review," *Injury*, vol. 53, no. 11, pp. 3575–3585, Nov. 2022.

[14] Y. Ye, T. Zhou, and J. Du, "Robot-assisted immersive kinematic experience transfer for welding training," *J. Comput. Civil Eng.*, vol. 37, no. 2, pp. 1–17, Mar. 2023.

[15] H. Li, L. Zhang, and K. Kawashima, "Operator dynamics for stability condition in haptic and teleoperation system: A survey," *Int. J. Med. Robot. Comput. Assist. Surg.*, vol. 14, no. 2, pp. 1–10, Apr. 2018.

[16] A. van der Schaft, *L_2-Gain and Passivity Techniques in Nonlinear Control* (Communications and Control Engineering Series), 3rd ed. Cham, Switzerland: Springer, 2017.

[17] J. E. Colgate and G. G. Schenkel, "Passivity of a class of sampled-data systems: Application to haptic interfaces," *J. Robot. Syst.*, vol. 14, no. 1, pp. 37–47, Jan. 1997.

[18] B. E. Miller, J. E. Colgate, and R. A. Freeman, "Guaranteed stability of haptic systems with nonlinear virtual environments," *IEEE Trans. Robot. Autom.*, vol. 16, no. 6, pp. 712–719, Dec. 2000.

[19] T. Hulin, A. Albu-Schäffer, and G. Hirzinger, "Passivity and stability boundaries for haptic systems with time delay," *IEEE Trans. Control Syst. Technol.*, vol. 22, no. 4, pp. 1297–1309, Jul. 2014.

[20] N. Colonnese and A. Okamura, "Stability and quantization-error analysis of haptic rendering of virtual stiffness and damping," *Int. J. Robot. Res.*, vol. 35, no. 9, pp. 1103–1120, Aug. 2016.

[21] J. J. Abbott and A. M. Okamura, "Effects of position quantization and sampling rate on virtual-wall passivity," *IEEE Trans. Robot.*, vol. 21, no. 5, pp. 952–964, Oct. 2005.

[22] N. Diolaiti, G. Niemeyer, F. Barbagli, and J. K. Salisbury, "Stability of haptic rendering: Discretization, quantization, time delay, and Coulomb effects," *IEEE Trans. Robot.*, vol. 22, no. 2, pp. 256–268, Apr. 2006.

[23] B. Hannaford and J.-H. Ryu, "Time-domain passivity control of haptic interfaces," *IEEE Trans. Robot. Autom.*, vol. 18, no. 1, pp. 1–10, Feb. 2002.

[24] J.-P. Kim and J. Ryu, "Robustly stable haptic interaction control using an energy-bounding algorithm," *Int. J. Robot. Res.*, vol. 29, no. 6, pp. 666–679, May 2010.

[25] J.-P. Kim, S.-Y. Baek, and J. Ryu, "A force bounding approach for stable haptic interaction," in *Proc. IEEE World Haptics Conf.*, Jun. 2011, pp. 397–402.

[26] F. B. Llewellyn, "Some fundamental properties of transmission systems," *Proc. IRE*, vol. 40, no. 3, pp. 271–283, Mar. 1952.

[27] J. E. Colgate, M. C. Stanley, and J. M. Brown, "Issues in the haptic display of tool use," in *Proc. IEEE/RSJ Int. Conf. Intell. Robots Syst.*, vol. 3, 1995, pp. 140–145.

[28] R. J. Adams and B. Hannaford, "Stable haptic interaction with virtual environments," *IEEE Trans. Robot. Autom.*, vol. 15, no. 3, pp. 465–474, Jun. 1999.

[29] A. Jafari, M. Nabeel, and J.-H. Ryu, "The input-to-state stable (ISS) approach for stabilizing haptic interaction with virtual environments," *IEEE Trans. Robot.*, vol. 33, no. 4, pp. 948–963, Aug. 2017.

[30] S. Kim and D. Y. Lee, "Control of haptic systems based on input-to-state stability," *IEEE Access*, vol. 10, pp. 27242–27254, 2022.

[31] H. Tugcan Dinc, T. Hulin, C. Ott, and J.-H. Ryu, "Relaxing conservatism for enhanced impedance range and transparency in haptic interaction," *IEEE Trans. Haptics*, vol. 17, no. 1, pp. 100–107, Mar. 2024.

[32] J. J. Gil, A. Avello, A. Rubio, and J. Florez, "Stability analysis of a 1 DOF haptic interface using the routh-hurwitz criterion," *IEEE Trans. Control Syst. Technol.*, vol. 12, no. 4, pp. 583–588, Jul. 2004.

[33] H. S. Woo and D. Y. Lee, "Exploitation of the impedance and characteristics of the human arm in the design of haptic interfaces," *IEEE Trans. Ind. Electron.*, vol. 58, no. 8, pp. 3221–3233, Aug. 2011.

[34] S. F. Atashzar, M. Shahbazi, M. Tavakoli, and R. V. Patel, "A passivity-based approach for stable patient–robot interaction in haptics-enabled rehabilitation systems: Modulated time-domain passivity control," *IEEE Trans. Control Syst. Technol.*, vol. 25, no. 3, pp. 991–1006, May 2017.

[35] S. F. Atashzar, M. Shahbazi, M. Tavakoli, and R. V. Patel, "A grasp-based passivity signature for haptics-enabled human–robot interaction: Application to design of a new safety mechanism for robotic rehabilitation," *Int. J. Robot. Res.*, vol. 36, nos. 5–7, pp. 778–799, Jun. 2017.

[36] A. Haddadi and K. Hashtrudi-Zaad, "Bounded-impedance absolute stability of bilateral teleoperation control systems," *IEEE Trans. Haptics*, vol. 3, no. 1, pp. 15–27, Jan. 2010.

[37] S. P. Buerger and N. Hogan, "Complementary stability and loop shaping for improved human–robot interaction," *IEEE Trans. Robot.*, vol. 23, no. 2, pp. 232–244, Apr. 2007.

[38] M. Minsky, O.-Y. Ming, O. Steele, F. P. Brooks, and M. Behensky, "Feeling and seeing: Issues in force display," *ACM SIGGRAPH Comput. Graph.*, vol. 24, no. 2, pp. 235–241, Mar. 1990.
[39] T. Hulin, C. Preusche, and G. Hirzinger, "Stability boundary for haptic rendering: Influence of physical damping," in *Proc. IEEE/RSJ Int. Conf. Intell. Robots Syst.*, Beijing, China, Oct. 2006, pp. 1570–1575.
[40] J. J. Gil, E. Sánchez, T. Hulin, C. Preusche, and G. Hirzinger, "Stability boundary for haptic rendering: Influence of damping and delay," *J. Comput. Inf. Sci. Eng.*, vol. 9, no. 1, pp. –1, Mar. 2009, Art. no. 011005.
[41] D. Cleveland and K. Hashtrudi-Zaad, "The effect of discretization techniques on uncoupled stability of haptic simulation systems," in *Proc. IEEE Haptics Symp. (HAPTICS)*, Mar. 2018, pp. 66–71.
[42] L. Pecly and K. Hashtrudi-Zaad, "Analog position estimation for enhanced stability and fidelity of haptic systems," *IEEE Trans. Haptics*, early access, Mar. 1, 2024, doi: 10.1109/TOH.2024.3371389.
[43] J. J. Gil, A. Ugartemendia, and I. Diaz, "Stability analysis and user perception of haptic rendering combining virtual elastic, viscous and inertial effects," *Appl. Sci.*, vol. 10, no. 24, p. 8807, Dec. 2020.
[44] A. Mashayekhi, S. Behbahani, F. Ficuciello, and B. Siciliano, "Analytical stability criterion in haptic rendering: The role of damping," *IEEE/ASME Trans. Mechatronics*, vol. 23, no. 2, pp. 596–603, Apr. 2018.
[45] A. Mashayekhi, M. Shakeri, S. Behbahani, and M. Keshmiri, "Describing function of the Gaussian friction model and its effect on stability of a haptic device," *J. Brazilian Soc. Mech. Sci. Eng.*, vol. 46, no. 3, pp. 1–11, Mar. 2024.
[46] A. Mashayekhi, S. Behbahani, F. Ficuciello, and B. Siciliano, "Influence of human operator on stability of haptic rendering: A closed-form equation," *Int. J. Intell. Robot. Appl.*, vol. 4, no. 4, pp. 403–415, Dec. 2020.
[47] T. Hulin, C. Preusche, and G. Hirzinger, "Stability boundary and design criteria for haptic rendering of virtual walls," in *Proc. 8th Int. IFAC Symp. Robot Control*, Bologna, Italy, Sep. 2006, pp. 322–327.
[48] R. Kikuuwe, N. Takesue, and H. Fujimoto, "A control framework to generate nonenergy-storing virtual fixtures: Use of simulated plasticity," *IEEE Trans. Robot.*, vol. 24, no. 4, pp. 781–793, Aug. 2008.
[49] S. A. Bowyer and F. Rodriguez y Baena, "Dissipative control for physical human–robot interaction," *IEEE Trans. Robot.*, vol. 31, no. 6, pp. 1281–1293, Dec. 2015.
[50] J. An and D.-S. Kwon, "Stability and performance of haptic interfaces with active/passive actuators—Theory and experiments," *Int. J. Robot. Res.*, vol. 25, no. 11, pp. 1121–1136, Nov. 2006.
[51] D. W. Weir, J. Edward Colgate, and M. A. Peshkin, "Measuring and increasing Z-width with active electrical damping," in *Proc. Symp. Haptic Interface Virtual Environ. Teleoperator Syst.*, Mar. 2008, pp. 169–175.
[52] A. Enoch, A. Sutas, S. Nakaoka, and S. Vijayakumar, "BLUE: A bipedal robot with variable stiffness and damping," in *Proc. 12th IEEE-RAS Int. Conf. Humanoid Robots*, Nov. 2012, pp. 487–494.
[53] S. Monteleone, F. Negrello, M. G. Catalano, M. Garabini, and G. Grioli, "Damping in compliant actuation: A review," *IEEE Robot. Autom. Mag.*, vol. 29, no. 3, pp. 47–66, Sep. 2022.

SHOULONG WANG received the B.S. degree in mechanical engineering from Donghua University (DHU), Shanghai, China, in 2015. He is currently pursuing the Ph.D. degree with the School of Mechatronics Engineering, Harbin Institute of Technology (HIT), Harbin, China.

His research interests include motor control, impedance/admittance control, and physical human–robot interaction.

JIE ZHAO (Member, IEEE) received the B.S. and Ph.D. degrees in mechatronics engineering from Harbin Institute of Technology (HIT), Harbin, China, in 1990 and 1996, respectively.

He is currently a Professor with the School of Mechatronics Engineering, HIT. He is the Leader of the Subject Matter Expert Group of Intelligent Robot in National 863 Program supervised by the Ministry of Science and Technology of China. His research interests include design, modeling and control of industrial robots, and bionic robots.

CHEN YANG (Member, IEEE) received the B.S. degree in industrial engineering and the M.S. and Ph.D. degrees in mechatronics engineering from Harbin Institute of Technology, China, in 2009, 2012, and 2017, respectively.

From 2013 to 2015, he was a joint Ph.D. Student with the Swiss Federal Institute of Technology in Lausanne, Switzerland. From 2017 to 2022, he was a Postdoctoral Associate and a Research Scientist with the Department of Mechanical Engineering, Massachusetts Institute of Technology, Cambridge, MA, USA. Since 2022, he has been a Principal Investigator with the ZJU-Hangzhou Global Scientific and Technological Innovation Center, Zhejiang University, China. His research interests include scanning probe microscopy, mechatronics, precision motion control, and their applications in ultra-precision manufacturing.

YANHE ZHU (Senior Member, IEEE) received the B.S. and Ph.D. degrees in mechatronics engineering from Harbin Institute of Technology (HIT), Harbin, China, in 1998 and 2004, respectively.

He is currently a Professor and a Ph.D. Supervisor with the School of Mechatronics Engineering, HIT. He is also the Deputy Director of the State Key Laboratory of Robotics and System. His research interests include reconfigurable modular robots and robotic exoskeletons.